

Computational electromagnetics for the SKA-Low prototype station AAVS2

Pietro Bolli^{a,*}, David B. Davidson^{b,*}, Mirko Bercigli^c,
Paola Di Ninni^a, Maria Grazia Labate^d, Daniel Ung^b and
Giuseppe Virone^e

^aNational Institute for Astrophysics, Arcetri Astrophysical Observatory, Florence, Italy

^bCurtin University, International Centre for Radio Astronomy Research, Perth,
Western Australia, Australia

^cIngegneria dei Sistemi, Pisa, Italy

^dSKA Observatory, Manchester, United Kingdom

^eNational Research Council, Institute of Electronics, Computer, and Telecommunication
Engineering, Turin, Italy

Abstract. We summarize the activities conducted since 2019 in the numerical electromagnetic analysis of one prototype station of the SKA-Low telescope. Working closely with the SKA Observatory, two teams based in Australia and Italy have collaborated effectively in modeling and analyzing AAVS2, which is the most recent prototype of an SKA-Low station installed in Western Australia. A comprehensive overview of the main electromagnetic parameters at element and array level obtained with two different commercial solvers is presented. Results for scattering parameters, individual element patterns, and station beams are shown; all these fully incorporate mutual coupling effects. Sensitivity of the station is addressed, as the cross-polarization performance. Finally, we also address some lessons learned and their impact on the project. © The Authors. Published by SPIE under a Creative Commons Attribution 4.0 International License. Distribution or reproduction of this work in whole or in part requires full attribution of the original publication, including its DOI. [DOI: [10.1117/1.JATIS.8.1.011017](https://doi.org/10.1117/1.JATIS.8.1.011017)]

Keywords: Square Kilometre Array; low-frequency aperture array; computational electromagnetics; mutual coupling.

Paper 21099SS received Aug. 29, 2021; accepted for publication Dec. 22, 2021; published online Jan. 18, 2022.

1 Introduction

As a part of the SKA-Low design process, several prototype stations have been deployed on the Murchison Radio-astronomy Observatory in Western Australia, to test a variety of aspects of the planned system. Known as the aperture array verification system (AAVS), several versions have been deployed, starting with the 16-element AAVS0.5 (circa 2013), moving onto the 256 element AAVS1 (2016 to 2017),¹ and finally to the 256 element AAVS2 deployed in 2019.² (The initial phase of AAVS2 deployment comprised three clusters of 16 elements each, known as AAVS1.5.) All these systems shared a quasi-random distribution of antenna elements; the elements themselves are log-periodic dipoles known as the Square Kilometre Array log-periodic antenna (SKALA) and these have also evolved with the various deployments; the elements in AAVS2 are SKALA4.1 antennas.³

A key part of the AAVS effort has been to provide reliable simulations of the detailed antenna pattern, including the effects of mutual coupling, to support comparison of the antenna designs proposed and installed in the various AAVS prototype stations, as well as preliminary astronomical tests. The groups in Italy [National Institute for Astrophysics (INAF)] and Australia [International Centre for Radio Astronomy Research-Curtin (ICRAR-Curtin)] performed Computational Electromagnetic (CEM) simulations on AAVS1.5 and AAVS2. The analysis is conducted with two different commercial full-wave simulation packages—FEKO from Altair⁴ and Galileo-EMT

*Address all correspondence to Pietro Bolli, pietro.bolli@inaf.it; David B. Davidson, david.davidson@curtin.edu.au

[†]These authors are the co-first authors.

(ElectroMagnetic Toolkit) from Ingegneria dei Sistemi⁵—both using the same underlying simulation modeling technique. These models have been compared and the results found to be consistent.^{6,7} Moreover, they have been validated against field measurements made during the campaign conducted by means of a RF-source installed on board an unmanned aerial vehicle (UAV).^{8,9}

This paper starts by reviewing the SKA-Low station and the antenna elements that comprise it. CEM analysis is briefly reviewed, with particular emphasis on the method of moments (MoM). The numerical models of a full station involve large numbers of degrees of freedom (several million are typical) and some of the most significant computational considerations are outlined. The scattering (S) parameter matrix is discussed and some results are shown. Central to contemporary array analysis is the inclusion of mutual coupling,¹⁰ which is done here using embedded element patterns (EEPs)¹¹—individual antenna patterns. Computed EEPs, as well as the differences of the EEPs computed by the two simulation packages (solvers) are presented. A statistical analysis of the computed EEPs is also described. Section 6 addresses the station beams (formed from a weighted sum of the individual patterns). At zenith, the station beam satisfies the phase 1 SKA-Low requirements, but some issues emerge as the station beam is electronically “scanned” off zenith. (Note that much antenna terminology derives from considering the antenna as a transmitter. Due to reciprocity, most antenna metrics, such as radiation patterns, are also valid on reception, such as a typical receive-only radio telescope.) This includes offsets in beam-steering angle and degradation in cross polarization. Two methods are proposed to ameliorate the beam-steering problem; one equalizes the phase, and another uses a beamforming technique known as maximum directivity (MAXDIR), leveraging knowledge of the EEPs. Two sections are then dedicated to provide numerical estimates for AAVS2 in terms of station sensitivity and polarization performance. This paper concludes by addressing lessons learned from the simulations for the SKA-Low telescope design.

Computational electromagnetic techniques are now mature, but the ability to routinely analyze structures of the electromagnetic size and complexity of a full SKA-Low station is relatively recent. SKA-Low will be the first aperture array of this type to have been rigorously simulated before deployment, and this is the main contribution of this paper.

2 SKALA4.1 Antenna and AAVS2 Station

The SKA demand for unprecedented sensitivity and bandwidth performance required the design of a quite complex antenna when compared to existing low-frequency aperture array radio telescopes such as the low-frequency array (LOFAR),¹² designed and built by ASTRON; the long-wavelength array (LWA),¹³ a joint collaboration of several universities and scientific research organizations based on the USA; and the Australian Murchison widefield array (MWA).¹⁴ All of these telescopes are based on dipole antennas, most with a bow-tie shape to increase the bandwidth (high-band LOFAR, LWA, and MWA). SKA-Low relies on an antenna comprising by a series of half-wave dipoles, known as log-periodic dipole array (LPDA).¹⁵ The design and optimization of this antenna (named SKALA) has taken several years and in the course of the project several versions have been proposed.^{16–18} The version selected as reference antenna during the SKA System Critical Design Review in December 2019 is the so-called SKALA4.1.³

The SKALA antenna consists of two identical orthogonal LPDAs to receive both linear polarizations of the electromagnetic waves emitted by the Universe. For AAVS2, the North–South polarization is labeled “Y,” and the orthogonal East–West polarization “X;” this nomenclature is used throughout this paper. The antenna is vertically mounted such that its maximum gain is directed toward the zenith direction. It also exhibits a large field of view (FoV) to capture waves up to 45 deg off zenith, which is the largest specified scan angle for SKA-Low, and even at lower elevations with reduced sensitivity. For each polarization, the SKALA4.1 antenna is formed by 20 dipoles with triangular shape, apart for the bottom dipole which features a bow-tie shape. On top of the antenna (2.1 m above the terrain), two single-ended 50-ohm low-noise amplifiers (LNAs) are installed inside the antenna booms. A metallic ground plane is deployed under the antenna to make the antenna response less sensitive to the variable terrain properties and to improve the zenith gain at lower frequency. In order to provide a discharge path for electrostatic charge build-up, the SKALA4.1 is electrically grounded to the metallic plane.

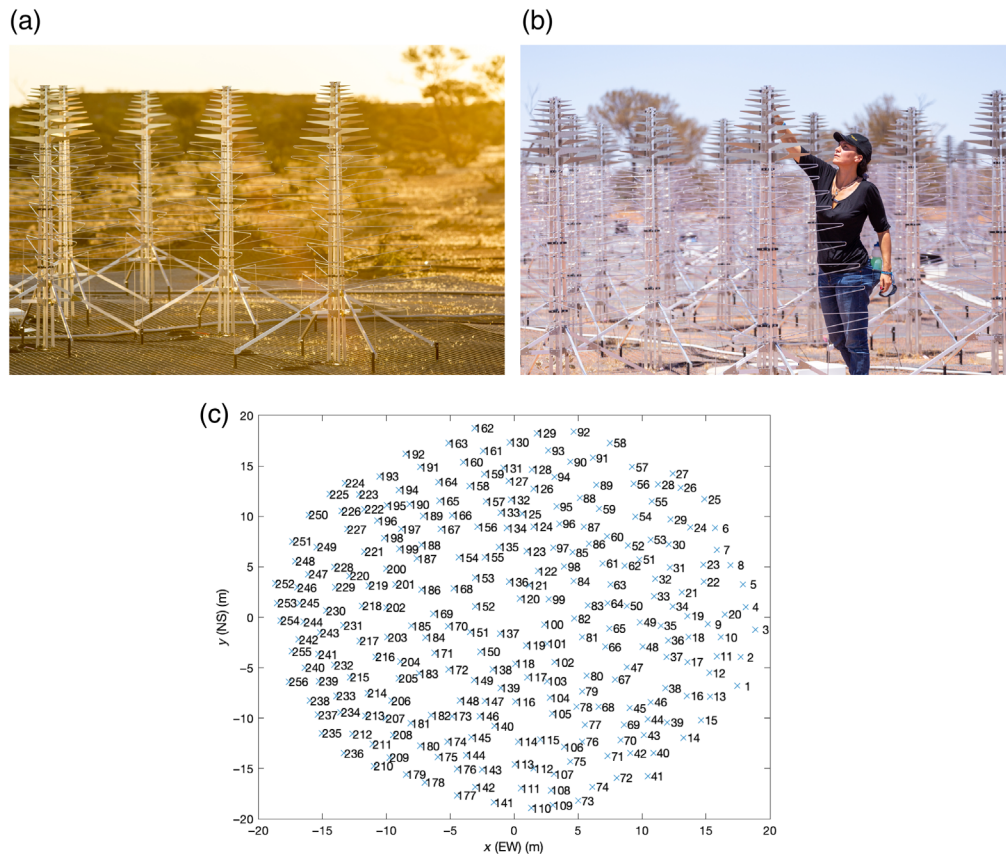


Fig. 1 Several views of the AAVS2 array. (a) The first phase of the array under construction in May 2019, showing the individual SKALA4.1 elements. (b) One of the authors (MGL) inspecting an installed SKALA4.1 and (c) a schematic of the antenna layout. Clearly visible is the quasi-random element layout. Credits: ICRAR/INAF.

After having successfully passed a series of mechanical and electromagnetic acceptance tests, the SKALA4.1 antenna was eventually fabricated by Sirio Antenne (Italy)¹⁹ in 256 units to populate the AAVS2 station (Fig. 1). This was conceived to verify the antenna performance in the real operating environment and including all the other components of the station, such as the preconditioning RF components, the optical fibers, and the digital acquisition backend. The installation of the antennas also gave the opportunity to learn lessons on the mounting procedures for further mechanical optimization.

The quasi-random layout of antennas in AAVS2 is displayed in Fig. 1(c) and is based on the distribution of AAVS1 but accounts for the larger dimensions of the SKALA4.1 antenna with respect to its predecessor SKALA2. The diameter of AAVS2 is 38 m (maximum distance between the antenna centers), while for AAVS1 it was 35 m. This also assures a reasonable walk-through to access every antenna. Due to the size of the antenna, the diameter is 40 m measured across the furthest antenna arms. The ground plane is 42 m in diameter.

Since 2019, AAVS2 has been available to the astronomical commissioning team for preliminary observations to characterize the array in terms of calibration, sensitivity, imaging, data stability, and repeatability. Early works include preliminary results on Sun and galaxy transit with a calibrated station,^{2,20} sensitivity verification studies,²¹ and an all-sky southern-hemisphere radio transient monitor.²²

3 Electromagnetic Analysis

Computational electromagnetics is a well-established field which numerically solves Maxwell's equations.²³ This includes both integral equation-based methods (the MoM) and differential

equation-based techniques, in particular the finite difference time domain method and the finite-element method. After many years of development since their introduction in the 1960s, simulation codes implementing these techniques are mature and in widespread use.

For modeling the highly conducting metallic antenna elements of aperture arrays, the MoM is a very competitive method. Most MoM codes, including FEKO and Galileo-EMT (hereafter referred to as Galileo only), the two used in this work, use a linear basis function to approximate the electric current along a wire filament, and a mixed order basis function defined on a triangular element to approximate surface current. (The latter was first published in the 1980s and is widely known as the RWG element after the initials of its originators.²⁴)

A prime consideration when modeling antenna arrays as complex as the AAVS systems is to generate a mesh that is sufficiently fine to adequately resolve both the geometry and the current distribution, but no finer, as the computational cost grows very rapidly with the number of unknowns. The MoM in its standard form has a memory requirement that grows as $\mathcal{O}(N_{\text{dof}}^2)$, and computational cost that grows as $\mathcal{O}(N_{\text{dof}}^3)$. N_{dof} is the number of mesh elements, or degrees of freedom, and for a thin-wire antenna is proportional to frequency; when surfaces are meshed, N_{dof} is proportional to the square of frequency. It will be appreciated that this cost rapidly becomes prohibitive, either as the antenna size or the frequency increases, or both. For electromagnetically large problems, the fast multipole method (FMM) (also known as the fast multipole algorithm), originally introduced in the mid-1980s to speed up the calculation of long-ranged forces in the n -body problem, was adapted to the iterative solution of MoM problems in the early 1990s;²⁵ combined with major advances in high-performance computing, it proved key to solving very large problems. In its multilevel form, the FMM becomes MLFMM and it has an asymptotic computational dependence of $\mathcal{O}(N_{\text{dof}} \log N_{\text{dof}})$ per iteration. Unfortunately, the iterative solver is not guaranteed to converge, and this becomes particularly problematic for low-frequency problems. Nonetheless, the MLFMM has become the standard for the discrete (i.e., meshed) solution of Maxwell's equations in integral form. FEKO was the first commercial code to include the MLFMM around 20 years ago; Galileo also includes an implementation of this technique.

Work continues on alternate approaches to fast solvers using variants of the FMM, which as noted above can demonstrate unpredictable convergence behavior. A number of these are based on the concept of characteristic basis functions,²⁶ also known as synthetic basis functions²⁷ and more generally as macrobasis functions (MBFs). This method uses high-level functions which are supersets, or agglomerations, of elementary basis functions such as the widely used divergence-conforming RWG triangular basis functions.²⁴ MBFs are chosen to exploit the physics of the electromagnetic interaction with the geometry of the structure. The overall aim is to greatly reduce the number of degrees of freedom required and permit direct solution of the resulting matrix equation. An early example of MBF application in radio astronomy is.²⁸ A specific application to SKA-Low is HARP; a description of the method and references to earlier work is provided in Ref. 29. However, this method has not been implemented to date in commercial codes. Another is the Domain Green's function approach;³⁰ FEKO supports an implementation of this. Unfortunately, in its original form, it is not well suited to the computation of EEPs. Work is currently in progress on addressing this.³¹ In summary, a number of promising methods exist in prototype form in research codes. However, when simulating something as complex as an SKA-Low station, properly verified and validated software is invaluable so methods already implemented in commercial codes such as FEKO and Galileo are preferred, even if computationally suboptimal.

Due to the increased number of dipoles, the SKALA4.1 is appreciably more complex to model numerically than its predecessor in the AAVS1, the SKALA2, not least in terms of the use of solid metal elements at the high-frequency end (which as noted above requires a large number of degrees of freedom to model). FEKO and Galileo models have been developed that retain sufficient fidelity to accurately predict antenna characteristics across the frequency range of interest, while allowing a reasonable computational time—especially for the full-station analysis.

The EM models have been implemented by starting from the as-built mechanical drawings of the SKALA4.1 antenna and simplifying some of the geometrical features. A comprehensive description of this process for FEKO may be found in Ref. 32. The model simplifications have

been conducted independently in FEKO and Galileo, which means that slightly different assumptions have been implemented. Nevertheless, as it will be shown in Sec. 5.2, good agreement is obtained between EEPs computed from the two data sets. The following simplifications are valid for both models.

- An infinite metallic ground plane is implemented in the model. This permits use of the reflection coefficient approximation technique. A preliminary analysis on the effects of a more realistic finite ground plane and also on the terrain properties have been published in Ref. 33. In that paper, the EEPs of antennas located in different positions of the station are computed with both an infinite and a finite (diameter of 42 m) ground plane to evaluate the differences between the two approaches. For the finite ground plane, different terrain properties were also considered. The EM analysis was based on a simplified procedure to compute the currents on the antennas assuming an infinite ground plane and then radiating them on a finite plane. A different way to compute, for rectangular ground plane cases, the radiation pattern of antennas installed on finite plane is presented in Ref. 34.
- No ohmic losses. Both the SKALA4.1 antennas and the ground plane have been modeled with perfect electric conductor (infinite electrical conductivity); this implies a radiation efficiency of 100%.
- All dielectric elements present in the antenna, such as spacers or support structures have been neglected by the analysis.
- Although the antenna ports are actually excited with a coaxial port, the models use a differential wire excitation (a “delta gap” model in MoM terminology). This has been verified to lead to very accurate results with respect to the coaxial port excitation.
- Some approximations in the antenna structure of the as-built model have been implemented, such as removing small plate structures toward the top of the antenna and other small details (e.g., access hole, bolts, and rivet) which did not provide electromagnetic functionality.

These simplifications reduce N_{dof} to around 10,000 unknowns (depending on the different model produced); by comparison, an initial model derived from CAD files required over 29,000 unknowns. At the low-frequency end, this has been further reduced to around 4000 unknowns using a coarse mesh within the FEKO models.

This number of unknowns is easily manageable on a typical workstation for a single antenna, but it makes the computational time lengthy when more antennas are included in the model as in AAVS1.5 (48 antennas) or even worse in AAVS2 (256 antennas). Typical run-times on a multi-core workstation for the full AAVS2 model range from several hours to many days per frequency point, depending on the rate of convergence of the MLFMM, and occasionally, frequencies are encountered where the iterations do not converge.

The EM analysis of the individual SKALA4.1 antenna has been conducted with very fine frequency resolution. On the other hand, the analysis conducted on AAVS2 has been done at few frequency points selected to assure a good coverage of the station performance across the operational frequency band. Table 1 lists the frequencies that have been analyzed in FEKO and/or in Galileo. Currently, the team is extending the EM analysis to finer frequency resolution analysis.^{35,36} This will permit us to assess the spectral smoothness performance of the station and improve calibration schemes using knowledge of the EEPs.

Table 1 Frequencies (MHz) for which full AAVS2 simulation has been performed at the time of writing. Each frequency has two sets of 256 EEPs and one 512 port scattering matrix associated with it.

Freq.	50	55	70... 77	80... 100	110	140	160	210	220	230	280	320	340	345	350
Galileo	X	X	Only 70 and 77	Only 80	X	X	X	X	X	X	X	X	X	X	X
FEKO	X	X	X	X	X	X	X	X	X	X	X	X	X	—	X

The EEPs are computed by feeding one element at a time, with all the other elements (including the orthogonal ports) terminated appropriately (50Ω for the SKALA4.1 antenna). These EEPs fully capture array mutual coupling^{11,37} and are potentially all different. As usually defined, the EEPs contain the geometric phase terms associated with the element phase center locations in the array. (This is sometimes loosely referred to as the array factor (AF), although the name is not entirely accurate in this context.) For efficiency when storing, these terms can be suppressed, but need to be restored when computing the array pattern. (As an example, the patterns computed for AAVS2 using FEKO do not include these phase terms; see Sec. 6 for further discussion.)

Depending on the EM solver, the EEPs computed have either 0.5 deg or 1 deg resolution in θ (angle off zenith) and in ϕ (azimuth angle). Each set of 512 EEPs requires around 2.5 Gbyte of storage at 0.5 deg resolution per frequency point. (Finer angular resolution can, of course, be readily obtained from the solvers, but at the cost of additional storage.)

4 Scattering Matrix

A first indication of the mutual coupling among the antennas can be extracted from the scattering (S) parameter matrix. Among other information, they give an indication on how much the reflection coefficient (and therefore the antenna impedance) of each antenna changes due to the mutual coupling and how much power is coupled among different antennas. From this matrix, the array mutual impedance or admittance matrices are readily obtained using well-known transformations from microwave network theory. Figure 2 shows, at four different frequencies (50, 70, 160, and 350 MHz), the amplitude of the reflection coefficient (S_{ii}) of every single antenna for both ports, respectively. From this figure, we notice that at highest frequency, the port connected to the X pol (EW) is better matched to 50 ohm than the Y pol port (NS). (The SKALA4.1 antenna is not exactly symmetric for the two polarizations due to a difference of 1 cm along the vertical direction in the two excitation lines.) Furthermore, the scatter of the reflection coefficients for the different frequencies depends by the intrinsic matching of the isolated antenna, which is very poor (> -5 dB) until 60 MHz and then, above 90 MHz, it is almost always < -10 dB (see Ref. 3, Fig. 6) and the strength of the mutual coupling, which decreases with the frequency. At 50 MHz, the mutual coupling is expected to be strong but, due to the low power radiated by the mismatched antenna, the reflection coefficients of each antenna are quite constant. On the other hand, at 350 MHz the antennas radiate more power due to the good matching condition, but the mutual coupling is now lower and the variation of the reflection coefficient is reduced.

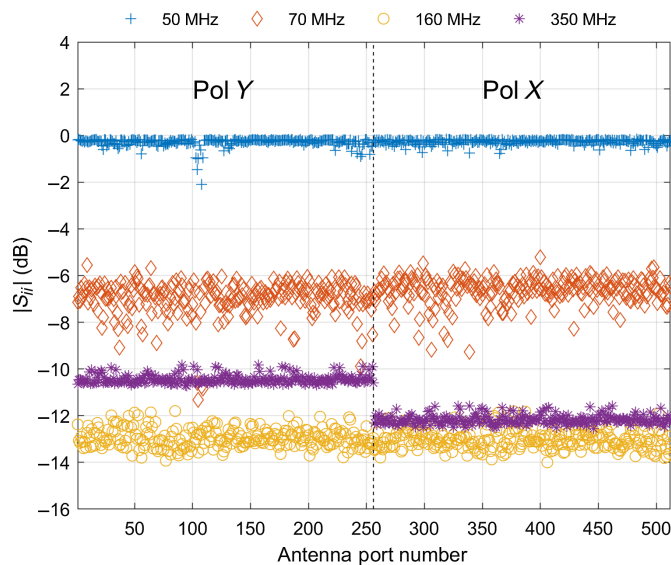


Fig. 2 Reflection coefficient of each antenna of AAVS2 at four different frequencies (50, 70, 160, and 350 MHz). The 256 antennas are divided in two groups: the first 256 ports refer to the Y polarization, while the others to the X polarization.

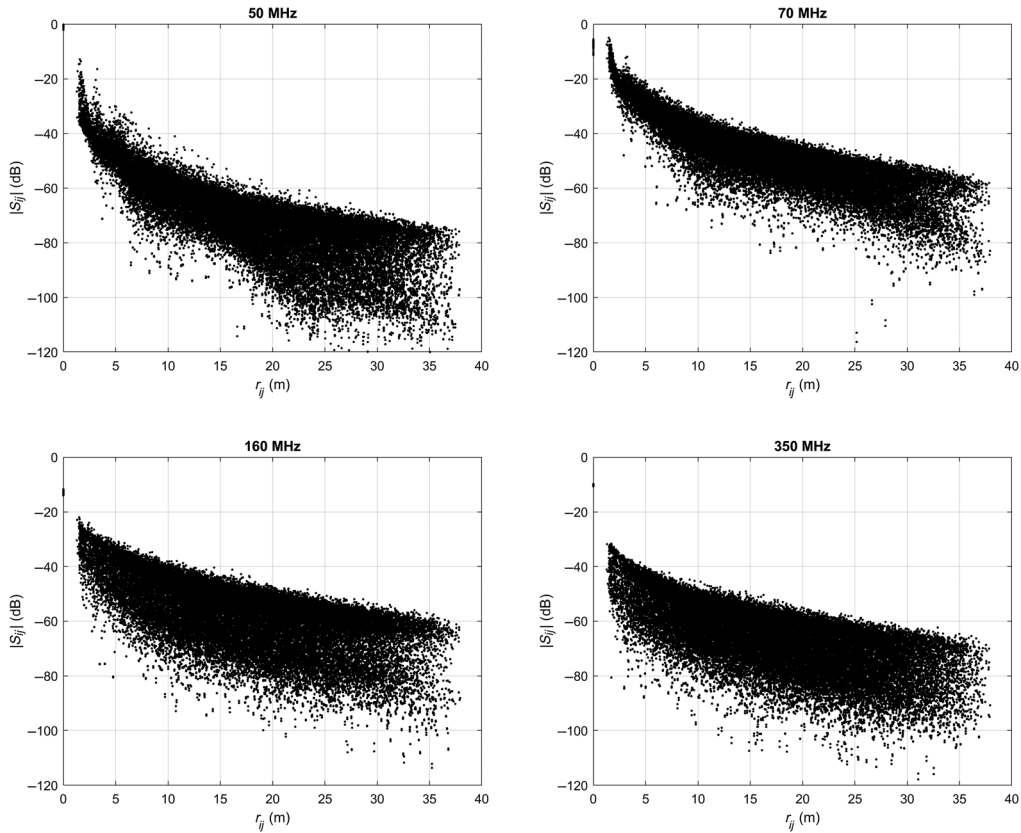


Fig. 3 Mutual coupling for every pair of antennas of AAVS2 at four different frequencies (only the polarization aligned to the Y axis is shown) expressed by the amplitude of the coefficients of the scattering matrix. The S_{ij} values are reported against the distance between each pair of antennas.

Indeed, among the four frequencies considered, the highest variability in the reflection coefficient occurs at 70 and 160 MHz where the combination of mutual coupling and good matching properties produces a scatter in the amplitude of the S_{ij} parameter.

For the same frequencies, we also plot in Fig. 3, for every possible pairs of antennas (i, j) (only for ports aligned along the Y axis), the amplitude of the S_{ij} parameter, which represents the coupling between two different antennas with all other antennas terminated on matched loads (50Ω terminations). The coefficients are plotted against the distance between the two antennas. Of course, for larger spacings, the coupling decreases. Overall, the slopes of the cloud distributions at 160 and 350 MHz are quite similar apart for a general shift toward lower values at 350 MHz. In particular, for pairs of antennas very close each other, the maximum of S_{ij} is reduced by almost 10 dB from 160 to 350 MHz. At 50 MHz, the mutual coupling is strongly influenced by the mismatching of the antenna; for antennas in close proximity, the S_{ij} can reach values up to almost -15 dB. Finally, 70 MHz shows significantly large coupling among the antennas (up to -5 dB).

Figure 3 also highlights another interesting aspect, that is the large variability (several tens of dB) of the coupling coefficient for the same distances of the antennas. This is caused by the different reciprocal alignments of the antennas that can be along either the principal planes or other directions.

5 Embedded Element Patterns

The dense distribution of the antennas plus the quite large dimensions of the individual SKALA4.1 antenna make the mutual coupling in a SKA-Low station significant, especially at low frequencies. Moreover, the aperiodic distribution of the antennas produces highly variable mutual coupling effects depending on the relative position of each antennas with respect to the

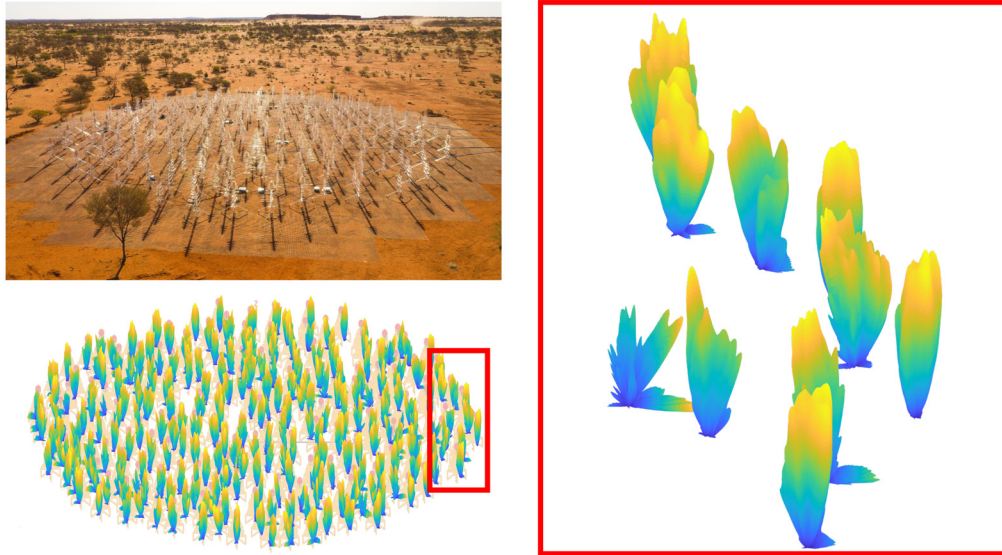


Fig. 4 A visualization of the EEPs at 75 MHz. The patterns are overlaid on the AAVS2 station, with (right) a blown-up view of some of the EEPs.

nearby antennas. This results in variation in the EEPs, which can be particularly critical at low frequencies, as shown in Fig. 4. This variability in the EEPs is assessed in Sec. 5.1 by introducing some figures of merit.

With such a large variability in the EEPs of SKA-Low, detailed knowledge of the EEPs becomes important for potential use in instrumental calibration process. However, this requires first validating the simulated EEPs with respect to the real antenna patterns. This was successfully done in 2019 by measuring the individual patterns of AAVS1.5 by means of a transmitting RF source installed on a UAV system.^{8,9} In addition to the experimental validation, one should also verify the robustness of the numerical models by comparing the EEP results obtained from independent EM codes. This latter is discussed in Sec. 5.2.

5.1 Statistical Analysis on the Diversity of the EEPs

For the two edges of the operating frequency band (50 and 350 MHz) and for an intermediate frequency (160 MHz), we show in Fig. 5 the EEPs of all antennas. Here we show only the amplitude of the EEPs, but of course the phase of the EEP is also affected by the mutual coupling. Owing to the symmetry of the antenna, the characteristics of the EEP here computed for the Y polarization would be very similar for the X polarization. As a reference, the plots include also the average of the EEPs (dashed curve) and the pattern for the isolated SKALA4.1 antenna (dotted curve). The pattern response of the SKALA4.1 resembles the dipole-like patterns with the H plane response wider than in the E plane (i.e., the plane parallel to the dipole elements). Moreover, the presence of the infinite ground plane imposes nulls at the horizon in the H plane (no electric field parallel to the ground can be supported by the metallic ground). On the other hand, for the E plane at the horizon, the electric field does not vanish and actually can reach quite large values. At 350 MHz, and only partially at 160 MHz, a spatial ripple is evident in the patterns which is caused by the superposition of the field directly radiated by the antenna and the component reflected by the ground plane. At 50 MHz, some patterns in the E plane suffer from deep nulls starting from 30 deg from the zenith direction. The EEP variability is quantified in the bottom subplots of Fig. 5 by the normalized standard deviation of the EEPs computed as

$$\epsilon(\theta) = 100 \frac{\text{std}(D_i(\theta))}{\max(\overline{D}_i(\theta))}, \quad (1)$$

where $\text{std}(D_i(\theta))$ is the standard deviation of all EEPs as a function of the zenith angle (along a specific azimuth plane) and $\max(\overline{D}_i(\theta))$ is the maximum value of the average of the EEPs in the

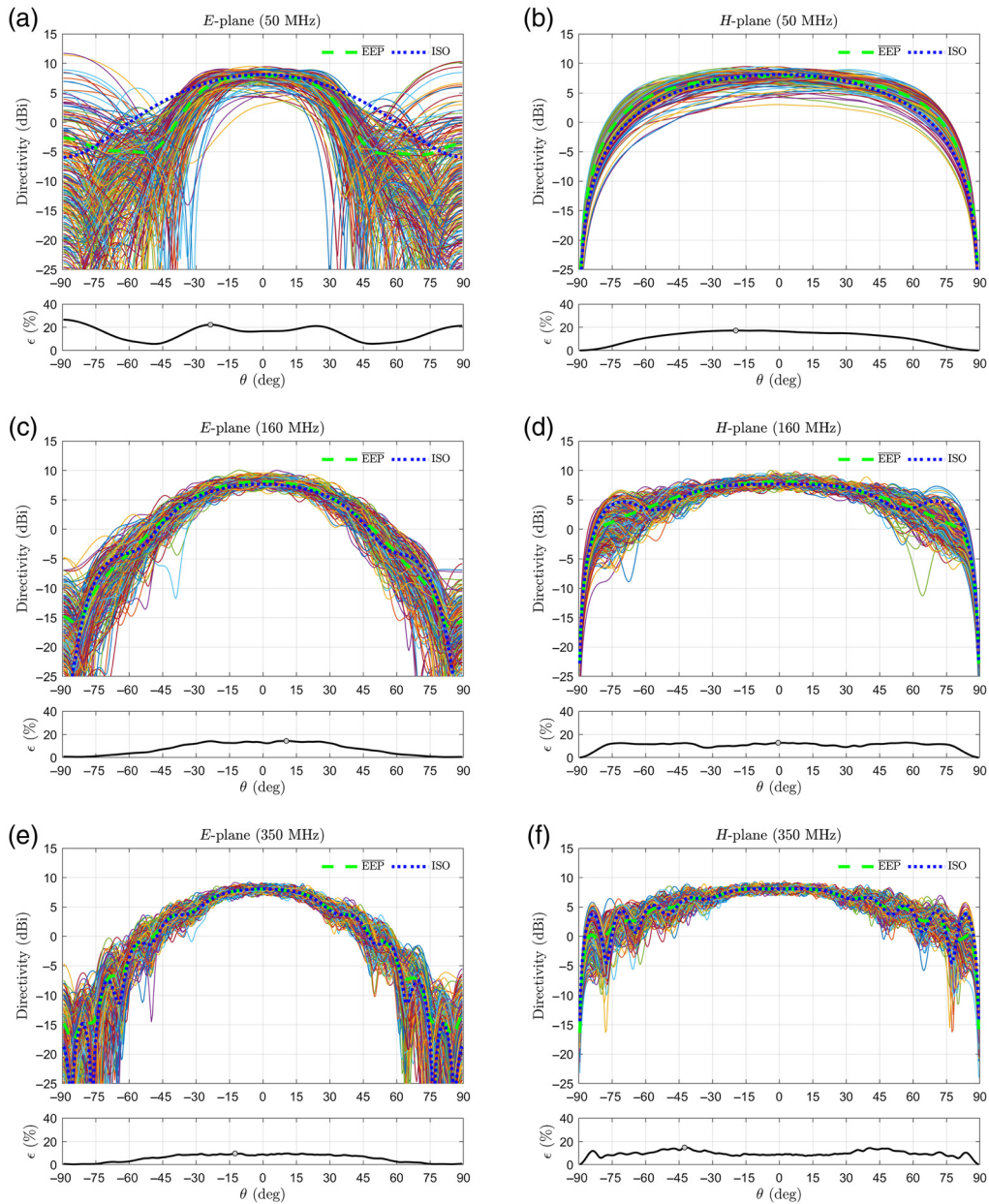


Fig. 5 Copolar directivity as a function of zenith angle for the 256 antennas comprising AAVS2. The excited port is aligned to the Y axis. (a), (c), (e) *E* plane and (b), (d), (f) *H* plane. (a), (b) 50 MHz; (c), (d) 160 MHz; and (e), (f) 350 MHz. The dashed and dotted curves represent the average of all directivity and the response of the isolated SKALA4.1 antenna, respectively. For each plot, the lower panel shows the normalized standard deviation of the directivities, whereas the circles show the zenith angle in which the standard deviation is maximum.

whole zenith range. The gray dot in the subplot of Fig. 5 shows the angular direction (within the antenna field of view) where the standard deviation reaches its maximum.

The general trend of the EEPs variability across frequency is described in Fig. 6 where the maxima of the normalized standard deviations in the two principal planes are shown for different frequencies. Both curves show a large standard deviation at lower frequencies with the *E* plane response always more distorted than the *H* plane. We also notice a noteworthy dependence of the standard deviation on the frequency. In particular, 55 and 80 MHz are the worst cases and a preliminary analysis has associated this couple of frequencies to some resonances in the antenna coupling.³⁵ Above 150 MHz, the standard deviation is always <15%, apart for one frequency point, but it never decreases below 10%.

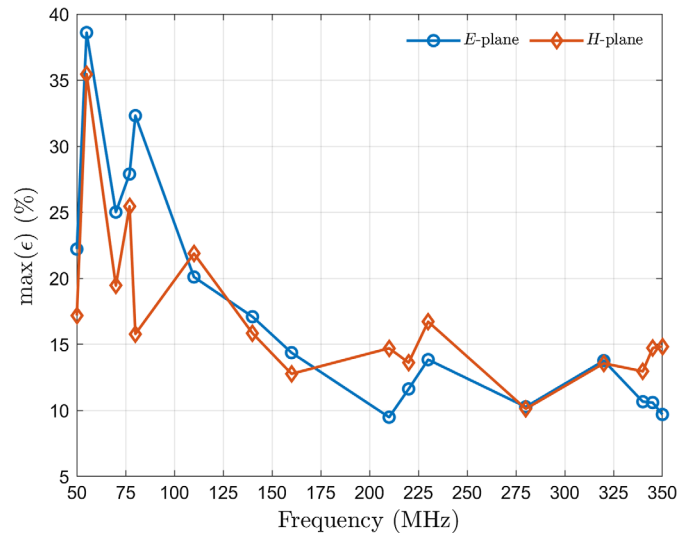


Fig. 6 Maximum of the normalized standard deviation for the EEPs of AAVS2 in the two principal planes.

An alternative representation of the variability of the EEPs is given for three different observation angles by the histograms of Fig. 7. For the three frequencies considered, we have grouped the antennas with directivity values within steps of 0.5 dB. Ideally, without mutual coupling, all antennas would have the same value of directivity, while in the real case, the antennas' directivities exhibit significant scatter. The histogram on the top refers to zenith direction and shows that at 350 MHz (yellow bars) 40% of the antennas comprising the AAVS2 station have directivity between 7.5 and 8 dBi, while slightly <40% have directivity in the upper range (8 to 8.5 dBi). At 160 MHz (red bars), about 80% of the antennas have directivities between 7.5 and 9 dBi. Finally, at 50 MHz (blue bars), the antenna directivities' scattering increases resulting in some antennas having zenith directivity as low as 3 dBi. The distribution of directivity is more spread for off-zenith directions and also shifted to lower values. For instance, Fig. 7(b) shows that for zenith angle of 45 deg in the *E* plane 90% of the antennas have a directivity at 50 MHz lower than 0 dBi; for this direction, at the other two frequencies, no more than 15% of the antennas have a directivity response that is included in a 0.5-dB wide bin. The plot for the *H* plane at 45 deg zenith angle [Fig. 7(c)] confirms that the drop in directivity is much less pronounced than in the *E* plane.

5.2 EEP Comparison Between FEKO and Galileo Data Sets

The FEKO and Galileo models of the SKALA4.1 antennas have been successfully verified in stand-alone conditions and shown in the previous papers: for instance, Fig. 6 of Ref. 3 compares the reflection coefficient of an individual SKALA4.1 antenna as simulated and measured, and Fig. 7 of Ref. 3 shows the directivity at zenith and at 45 deg off-zenith computed with different EM solvers. Also the results of AAVS2, therefore including the mutual coupling, have been described in previous works, for instance in Fig. 2 of Ref. 3, a comparison of the EEP for one antenna of AAVS2 using FEKO and Galileo is shown at different frequencies (80, 110, 160, and 350 MHz).

However, a meaningful and statistical analysis of the consistency between the two data sets has never been carried out. This is addressed here by evaluating for each antenna, the difference between the EEPs computed with FEKO and Galileo and normalizing this with respect to the average of the FEKO and Galileo values. In this computation, the squared magnitude of the EEP is used, so the difference is effectively in directive gain. This is computed across the common frequencies as listed in Table 1 and for three different observation directions. These normalized differences are then averaged over the 256 antennas at each frequency. Figure 8(a) shows the mean of the difference versus frequency at zenith. The results are much as expected. The

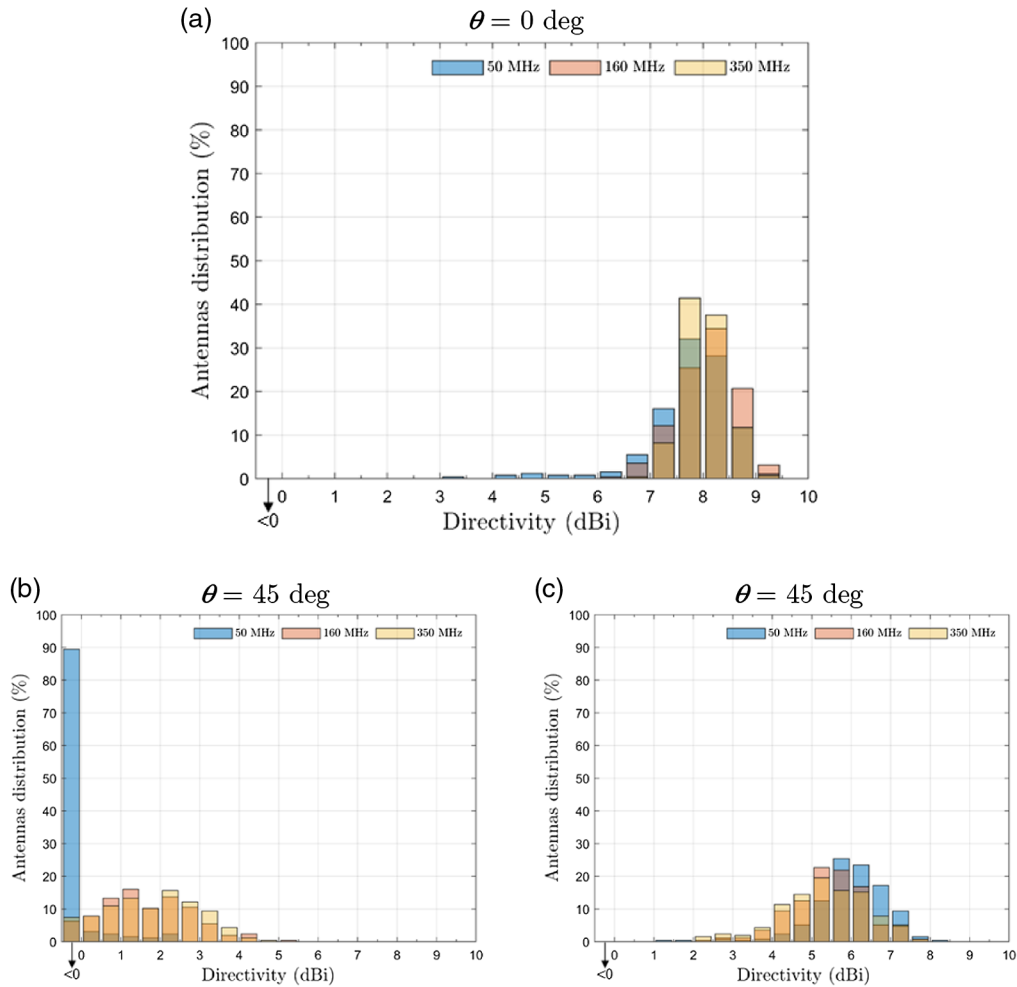


Fig. 7 Histogram distribution of the directivities for AAVS2 at 50, 160, and 350 MHz. Each bin represents the percentage of the antennas with directivity in steps of 0.5 dB from <math><0</math> to 10 dBi (the extreme left-hand bin groups all antennas with directivity <math><0</math> dBi). Directivity at (a) zenith direction and at 45 deg in the (b) *E* plane and (c) *H* plane.

differences are generally within a few percent (which translates to about a few tenths of a dB in terms of directive gain), except at 55 and 77 MHz, where the discrepancies between FEKO and Galileo data sets are more significant due to resonances in the antenna behavior produced by mutual coupling.³⁵ The differences in each polarization are shown separately; these are quite similar at each frequency. Figure 8(b) repeats this analysis for the *E* plane at 45 deg off-zenith and Fig. 8(c) for the *H* plane. The trends are very similar in all three plots, but the differences are generally around twice as large in the *E* plane.

These errors are better appreciated in Fig. 9, which compares the directivity of each EEP at zenith at 50, 55, 160, and 340 MHz for the FEKO and Galileo simulations. Some small variations are noted at 50 MHz; 55 MHz shows a dramatic variation in directivity,³⁵ and FEKO and Galileo results show largely oscillating values with differences for many antennas. At 160 and 340 MHz, the gain values largely cluster between 7 and 9 dBi and FEKO and Galileo results agree well.

6 Station Patterns

The straightforward way to compute the AAVS2 station beam is the simple geometric-based AF approach, as used in traditional array analysis and design. This approach uses the isolated (or potentially, the average if EEPs are available) pattern of the SKALA4.1 antenna multiplied by the AF, which accounts for the geometrical offsets between antennas.

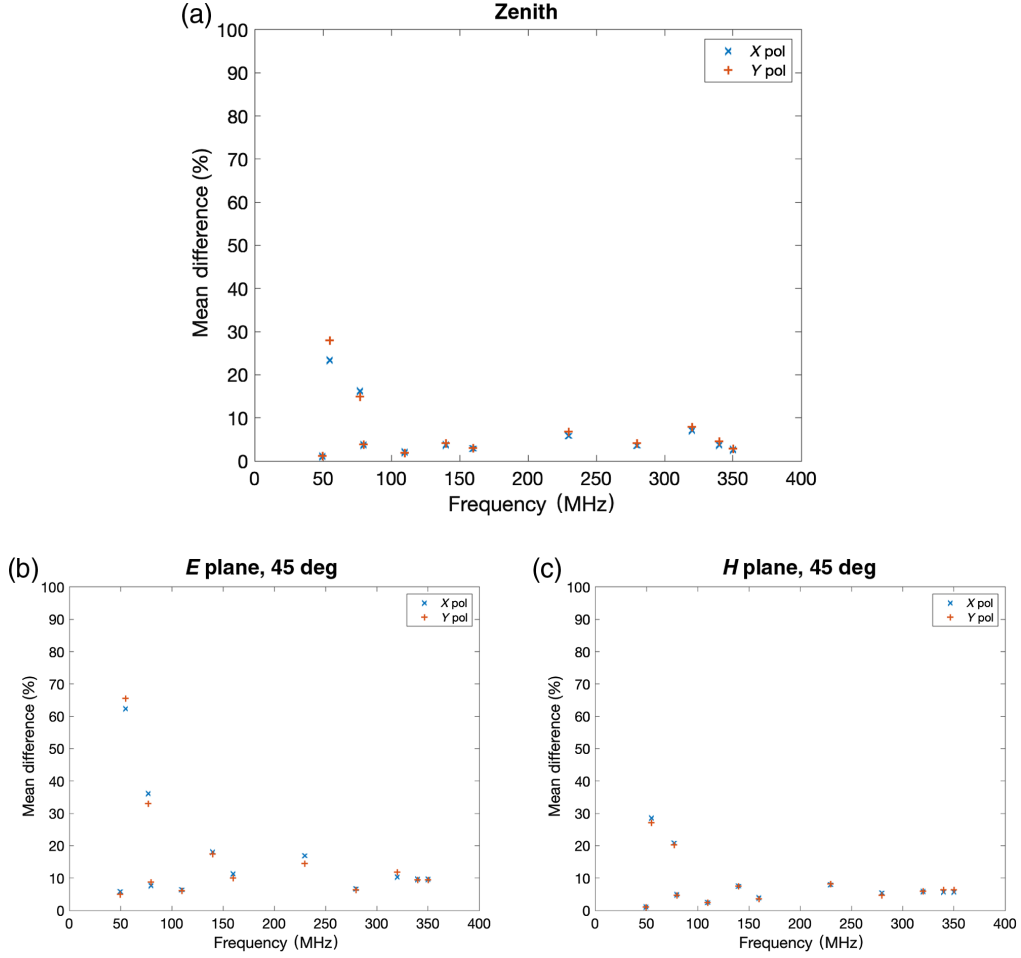


Fig. 8 Percentage differences between the EEPs computed with FEKO and Galileo for different frequencies. The difference is evaluated at (a) zenith and at 45 deg off zenith in the (b) E plane and (c) H plane.

For a multidimensional array comprising N antennas (see the presentation in Sec. 3.7 of Ref. 38 but with the dual-numbering scheme used there for a rectangular array replaced with a single-index appropriate for the quasi-random layout of AAVS2), the AF is given by

$$\text{AF}(\theta, \phi) = \sum_{n=1}^N i_n e^{jk(\hat{r} \cdot \vec{r}'_n - \alpha_n)}. \quad (2)$$

The prime is used to distinguish source coordinates from observation point coordinates. i_n is the current amplitude at the feed point of the n 'th element. If the array is planar, in the xy plane (as is the case with AAVS2), then

$$\text{AF}(\theta, \phi) = \sum_{n=1}^N i_n e^{jk(\xi_n - \alpha_n)}, \quad (3)$$

where

$$\begin{aligned} \xi_n &= \hat{r} \cdot \vec{r}'_n = [x'_n \sin \theta \cos \phi + y'_n \sin \theta \sin \phi], \\ \alpha_n &= [x'_n \sin \theta_0 \cos \phi_0 + y'_n \sin \theta_0 \sin \phi_0]. \end{aligned} \quad (4)$$

Here (θ_0, ϕ_0) is the main beam pointing direction, and the element coordinates are (x'_n, y'_n) for element n . If the array is uniformly fed (or weighted), then $i_n = 1$. The angle α_n is the phase

difference (relative to the origin) at element n required to steer the main beam to (θ_0, ϕ_0) . This is commonly known as the progressive phase delay, but this term is strictly speaking only applicable to a uniformly spaced array.

Therefore, the traditional AF approach is summarized by the following, which gives the array fields as a function of isolated pattern (\vec{E}_{iso}) and the AF:

$$\vec{E}(\vec{r}) = \vec{E}_{\text{iso}}(\vec{r})AF(\theta, \phi), \quad (5)$$

where \vec{r} is the vector to the field point, given in spherical coordinates by (r, θ, ϕ) . In the far field, only the angular variation is significant, and the isolated pattern is often computed at a nominal distance r . We return to this subsequently.

In Eq. (5), the AF multiplies the element factor, assumed to be the same for all elements. It is also worth mentioning that typically the array beam is steered by changing only the phase and keeping the amplitudes the same. (An amplitude taper may well be applied to control sidelobe level but generally will not change with scan angle.)

The simple geometric-based AF approach with isolated element pattern has limited accuracy, primarily because it ignores both mutual coupling and the variability in element patterns. In particular, it becomes progressively less reliable as scan angle off zenith increases

A more accurate model of the station, which takes into account the antenna interactions, is given by computing a different element pattern for each antenna (\vec{E}_n)—the EEP. These depend on the terminating impedances on all the nonfed antennas. A widely used choice, and that used in this paper, is impedance-match terminated ($Z_g = 50 \Omega$ for the SKALA4.1). The radiated field of the array is given by³⁷

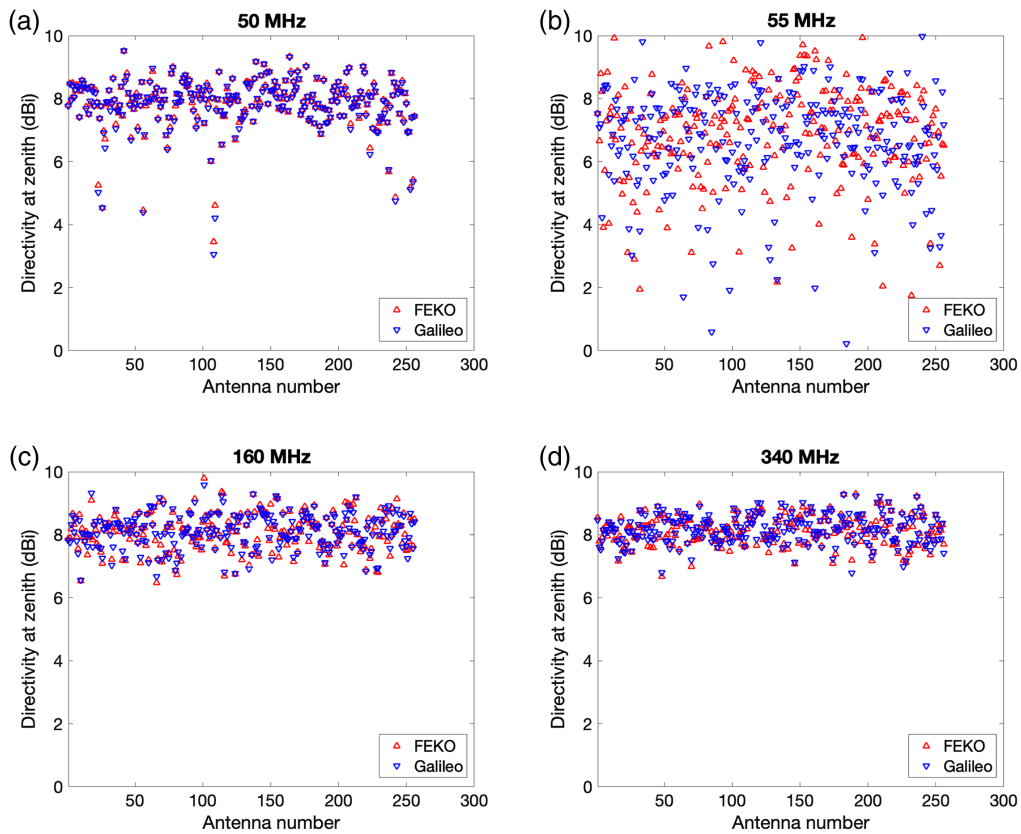


Fig. 9 Directivity at zenith for all the EEPs (Y polarization), computed at (a) 50 MHz, (b) 55 MHz, (c) 160 MHz, and (d) 340 MHz by FEKO and Galileo.

$$\vec{E}(\vec{r}) = \sum_{n=1}^N v_n \vec{E}_n(\vec{r}) e^{jk(\xi_n - \alpha_n)} \quad (6)$$

in terms of feed voltages and impedance-match terminated EEPs. Note that this is the Thevenin equivalent feed voltage not the port voltage. Mutual coupling, via the array mutual impedance matrix, connects the feed and port voltages, and port currents; this is discussed in more detail in the [Appendix](#).

For receive-only arrays, such as AAVS2, the reception pattern is given by the same result as Eq. (6), but with the feed voltage replaced by the beamformer weight. Again, this and some other subtleties of EEPs are discussed in the [Appendix](#).

6.1 Zenith and Off-Zenith Array Directivity

Following the comparison between the EEPs computed by Galileo and FEKO presented in Sec. 5.2, Fig. 10 shows the station beams obtained from the EEPs computed by the two solvers. Partial directivities [Ref. 11, Sec. 4.8.2] for the Y polarized ($N - S$ axis) antennas are shown for the co- and cross-polarized components. The fractional differences shown are normalized to the peak co-polar directivity, to avoid unduly emphasising errors in regions of very low field value. The agreement both in the co- and cross-polar is remarkable, considering that the simulations used different codes and different “meshes” to describe the antennas. It is also worth mentioning the significant reduction in the difference between the two data sets from the EEPs (Fig. 8) to the station pattern (Fig. 10).

Figure 11 shows the normalized cuts in the principal E plane for three frequencies for two steering directions (zenith and 45 deg from zenith in the E plane). This analysis is repeated both for the simplified (AF) and for the rigorous (EEPs) approach, and Fig. 11 shows that despite the strong mutual coupling affecting the EEPs, at station beam level the randomization of the layout mitigates the EEP variability; the simplified AF quite accurately reproduces the rigorous approach, especially around the main beam and first sidelobe. This is no longer true at 50 MHz for the 45-deg off zenith case where a quite large discrepancy between the two approaches is noted (and highlighted by the normalized error percentage reported below the plot).

The MAXDIR and the half-power beam-width (HPBW) of the AAVS2 station beam pointing at zenith vary from 25.8 dBi and 9.0 deg, respectively, at 50 MHz to 32.1 dBi and 1.2 deg at 350 MHz.

Finally, the directivity of AAVS2 is computed for every possible direction in the sky by adjusting the α_n phase coefficients defined in Eq. (4). The UV maps of Fig. 12 show the values of the station directivity at every nominal direction of the desired pointing. It is important to notice that these maps are computed by extracting the directivity at the nominal pointing directions, which does not necessarily correspond to the real maximum of the station. The maps are computed for both polarizations so that it is possible to appreciate the elliptical shape of the beam due to the asymmetry of the SKALA4.1 pattern between E and H planes. The color bars are kept constant throughout the three different frequencies to emphasize that directivity values are very similar at 160 and 350 MHz (i.e., in the sparse regime) while they are significantly reduced at 50 MHz (dense regime). At the angular limit of the FoV of SKA (represented by magenta circles), the reduction in the sensitivity with respect to the zenith value is lower than 3 dB in the H plane, while it increases to more than 6 dB in the E plane. This is valid for all frequencies and is due to the single antenna response. The maps at 50 MHz show the presence of an angular region in the E plane just outside the FoV where the synthesized beam features a quite deep null. This blind angle will be addressed in more detail in the next section.

6.2 Improving the Station Beam

In the previous section, the station beams have been computed by applying the basic techniques for array—either Eq. (5) or Eq. (6). Methods are now available which offer more sophisticated approaches.¹¹ This paper outlines in Secs. 6.2.1 and 6.2.2 some of the simpler such as phase-element calibration or the MAXDIR beamformer.

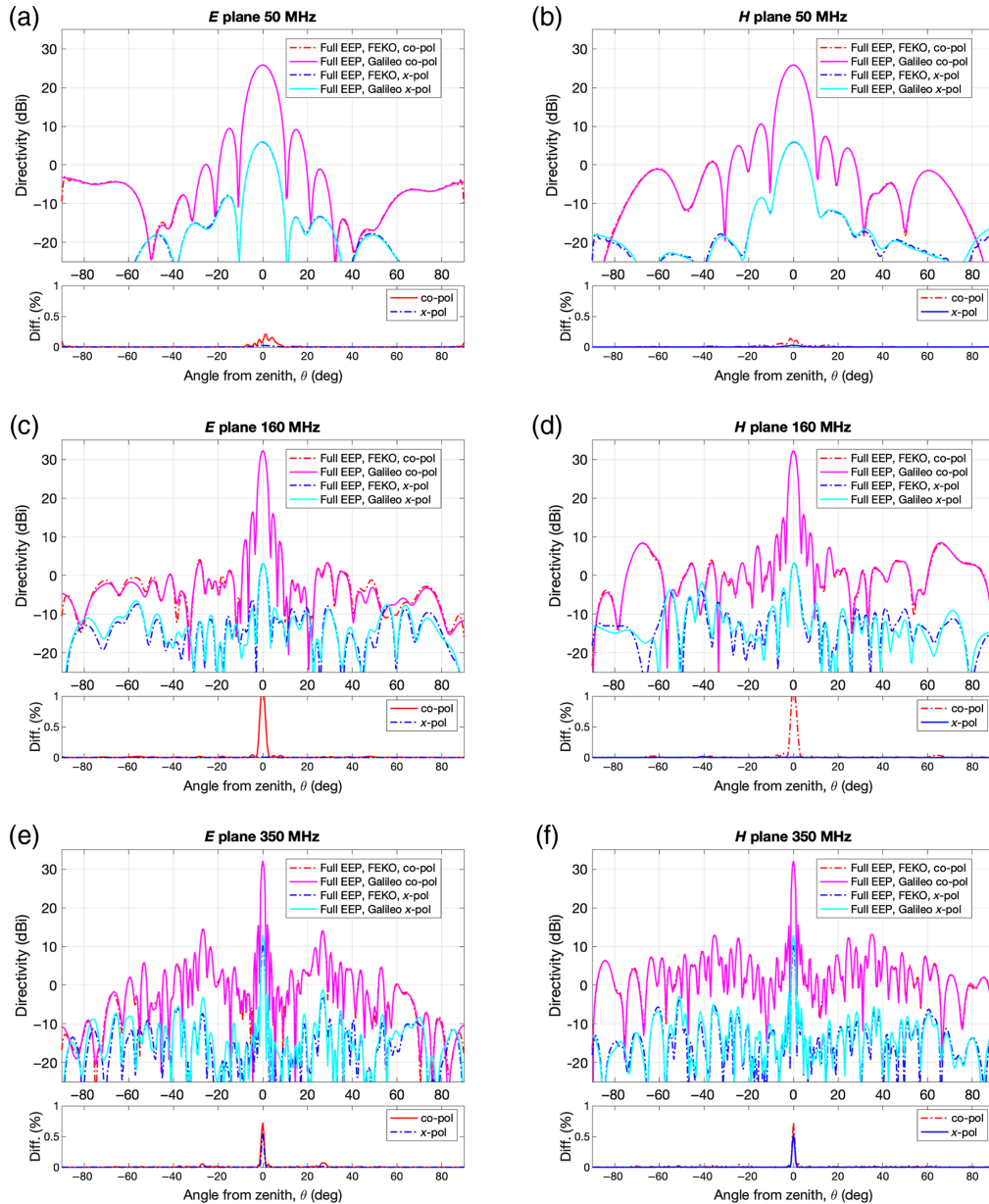


Fig. 10 Station (co-polar and cross-polar) directivity computed from Galileo and FEKO simulations for the Y polarized antenna. (a), (c), (e) *E* plane and (b), (d), (f) *H* plane. (a), (b) 50 MHz; (c), (d) 160 MHz; and (e), (f) 350 MHz. For each pattern, the bottom panel shows the normalized difference (%) as a function of the zenith angle.

6.2.1 Phase equalization for mutual coupling compensation

As shown in Fig. 5, the mutual coupling in pseudo-random array results in large variability of the amplitude of EEPs. Similar effects apply also to the phase component of EEPs. Such phase variability would produce a residual error in the phase terms when summing up the individual contribution to synthesize the station beam.

However, by exploiting the knowledge of the EEPs, it is possible to add to each antenna a phase term that equalizes the phase of the (co-polar) EEP along the desired pointing direction. In this way, all antennas will have the same phase contribution in the desired direction (see also Sec. IV in Ref. 39). This method is known as conjugate field matching in the signal processing literature.⁴⁰ By applying this technique, Eq. (6) is replaced by

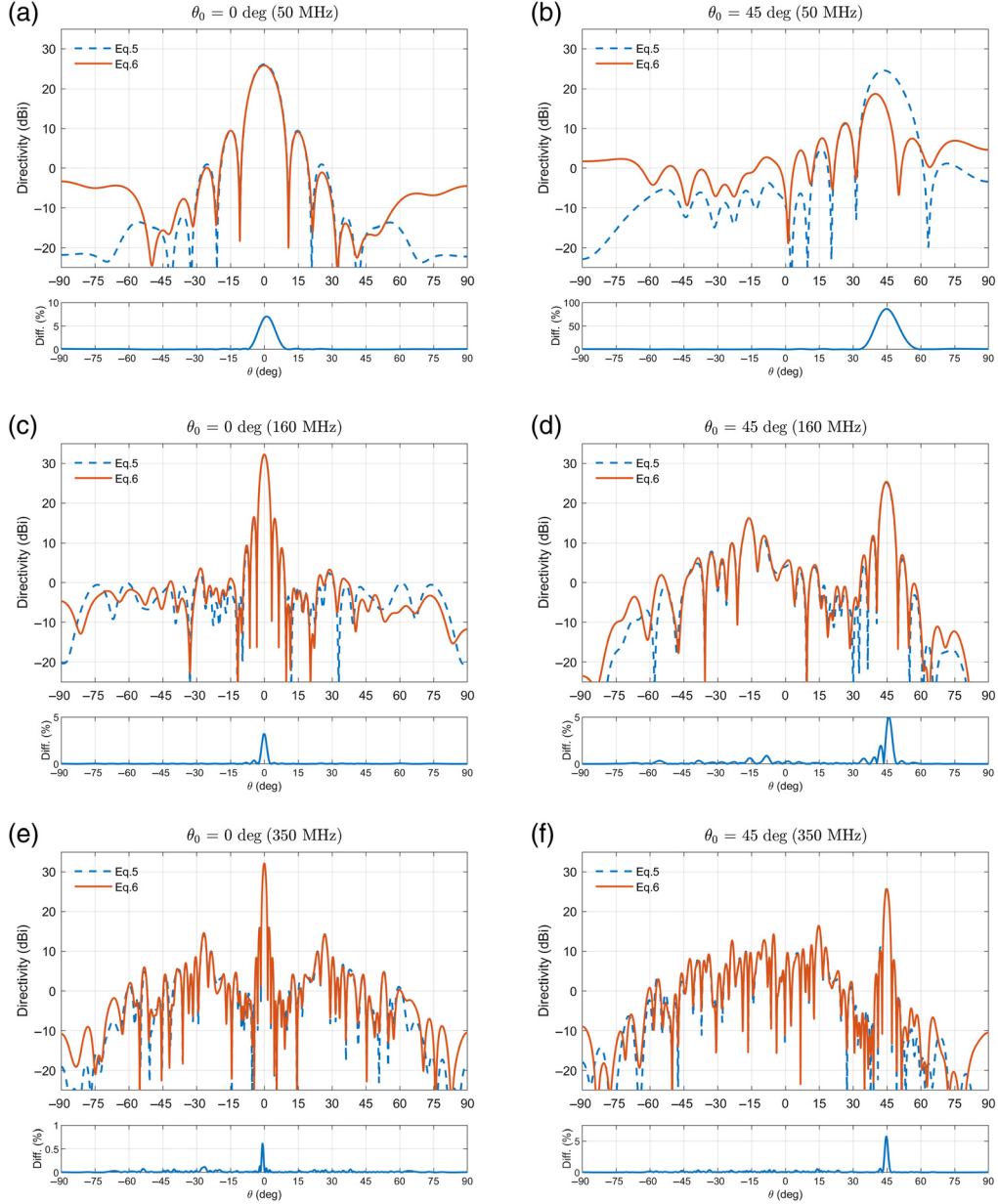


Fig. 11 Station co-polar directivity as a function of angle from zenith for AAVS2. The excited port is aligned to the Y axis. Pointing direction at (a), (c), (e) zenith and (b), (d), (f) 45 deg zenith angle in the E plane. (a), (b) 50 MHz; (c), (d) 160 MHz; and (e), (f) 350 MHz. The curves with dashed lines are computed using the isolated SKALA4.1 pattern [Eq. (5)], while the continuous lines are based on the EEPs [Eq. (6)]. For each pattern, the bottom panel reports the normalized difference (%) as a function of the zenith angle.

$$\vec{E}(\vec{r}) = \sum_{n=1}^N v_n \vec{E}_n(\vec{r}) e^{j(\xi_n - \alpha_n - \psi_n)}, \quad (7)$$

where ψ_n is the phase contribution of each co-polar EEP in the observing direction (θ_0, ϕ_0) .

We now consider this theory applied to the AAVS2 SKA-Low prototype array. Figure 13 shows the station beam formed by the traditional phase-only steering as in Eq. (6), and also the beam produced using the phase equalization as in Eq. (7). This figure compares directive gain patterns in the E plane for the $\theta = 45$ deg scan at two different frequencies. At 50 MHz, the phase equalization technique allows more than 1 dB of directivity to be recovered in the station

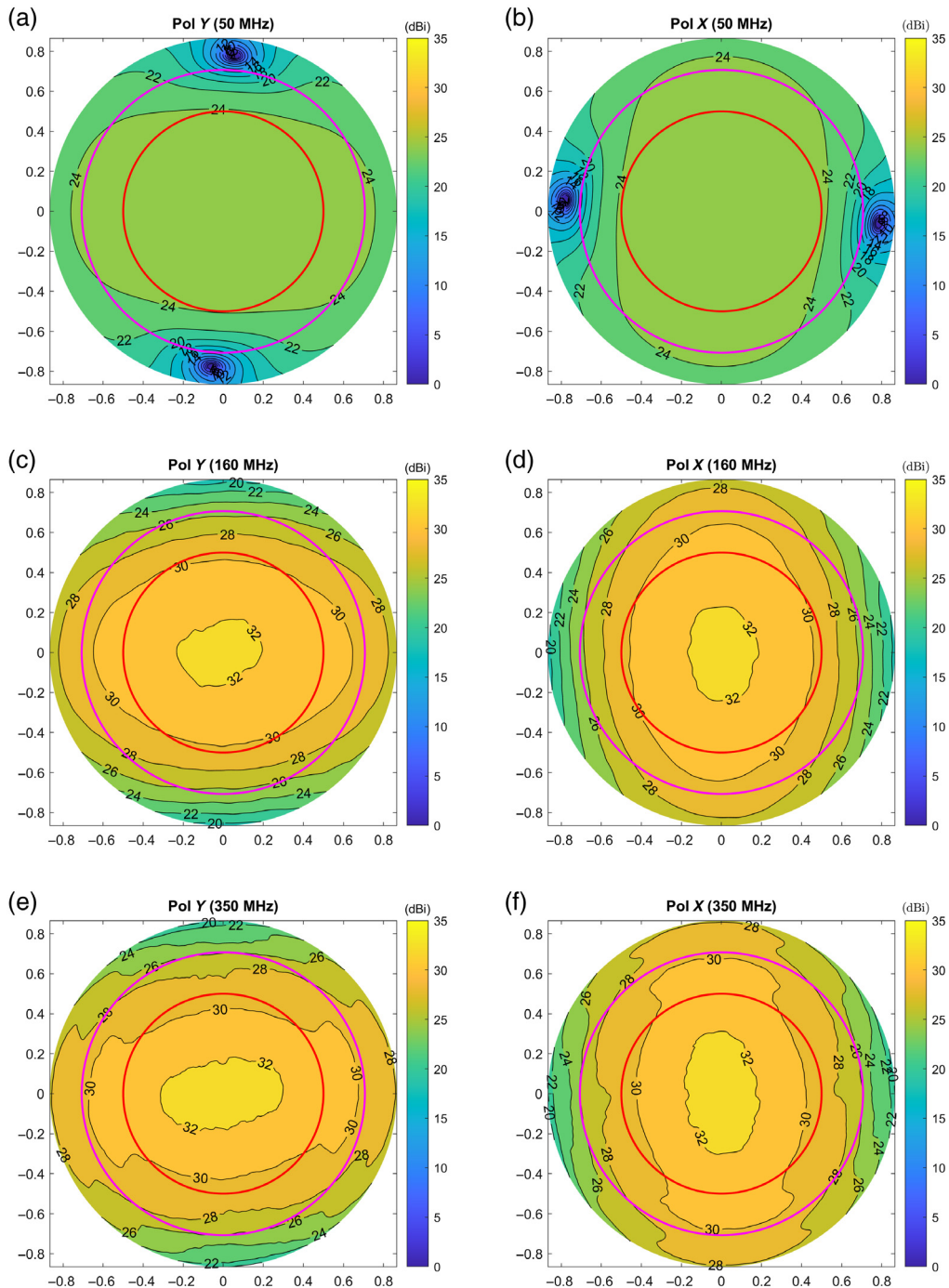


Fig. 12 UV maps of the station power (including both field components) directivity computed by steering the array beam in every direction of the sky and extracting the value at each pointing direction. The excited port is aligned with the Y axis for the left column and with the X axis for the right column. (a), (b) 50 MHz; (c), (d) 160 MHz; and (e), (f) 350 MHz. The UV maps are computed up to 60 deg of zenith angle, while the red and magenta circles indicate the zenith angle of 30 deg and 45 deg, respectively. The isocurves are given with a step of 2 dB.

beam [red curve against black curve in Fig. 13(a)] and also a slight reduction in the difference between the nominal and the actual pointing direction.

Figure 13(b) provides the same results for 70 MHz. It is apparent that the squint and loss of directivity are already far less serious at 70 MHz. This reflects the greater physical spacing between the active parts of the SKALA4.1 antennas, which, combined with a shorter wavelength, reduces the mutual coupling. This trend continues as the frequency increases.

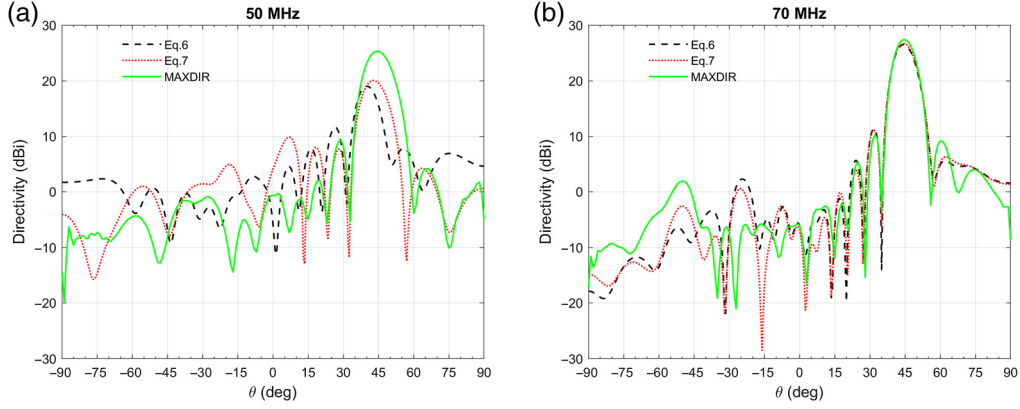


Fig. 13 A comparison of directivity for AAVS2 as a function of angle from zenith for two calibration station beamforming methods: MAXDIR and phase equalization [Eq. (7)], with respect to the standard EEP approach [Eq. (6)]. Plots refer to the Y polarization in the E plane at (a) 50 MHz and (b) 70 MHz. Nominal steering angle 45 deg in the E plane.

In the H plane (not shown), both the squint and the loss of directivity are far less noticeable. At its simplest, this is because the array elements are not foreshortened with scan angle in this plane (since the scan angle is perpendicular to the dipole array).

6.2.2 Maximum directivity beamformer

Equation (6) can be also written in a more compact form as

$$\vec{E}(\vec{r}) = \sum_{n=1}^N w_n \vec{E}_n(\vec{r}). \quad (8)$$

It is important to note that the complex-valued weight vector \mathbf{w} is not constrained to phase only, and indeed, quite general weight vectors could readily applied in digital receive-only arrays such as AAVS2. The conjugated weight is a convention in the beamforming literature [Ref. 11, Sec. 4.7.2]. Also note that the EEPs in this equation now include the geometric phase offsets.

By combining the total radiated power and the power density as outlined in Eq. (4.63) of Ref. 11, the total directivity can be expressed in matrix form as

$$D(\theta, \phi) = \frac{4\pi r^2 \mathbf{w}^H \mathbf{B}(\vec{r}) \mathbf{w}}{\mathbf{w}^H \mathbf{A} \mathbf{w}}. \quad (9)$$

The H superscript is the Hermitian (complex conjugate) transpose. \mathbf{B} is the array signal response matrix, with elements

$$B_{mn}(\vec{r}) = \frac{1}{2\eta_0} \vec{E}_m(\vec{r}) \cdot \vec{E}_n^*(\vec{r}), \quad (10)$$

It is computed from the EEPs in the direction of the desired scan angle, and as such, is angle-dependent. η_0 is the wave impedance of free space. \mathbf{A} is the pattern overlap matrix, with elements given by

$$A_{mn} = \frac{1}{2\eta} \int \vec{E}_m(\vec{r}) \cdot \vec{E}_n^*(\vec{r}) r^2 \sin \theta d\theta d\phi. \quad (11)$$

The $*$ superscript is the complex conjugate. The integral extends over the full sphere in general; for an array on highly conducting ground plane such as AAVS2, then only over the upper hemisphere. The dimension of these matrices is $N \times N$, where N is the number of array elements.

It can be shown [Ref. 11, Sec. 4.9] that a set of beamformer weights that optimizes directivity in a particular direction (and hence effective receiving area) can be obtained from the generalized eigenvalue problem:

$$\lambda \mathbf{A} \mathbf{w} = \mathbf{B} \mathbf{w}. \quad (12)$$

Directivity is optimized by choosing the maximum eigenvalue λ_{\max} ; the corresponding eigenvector is the desired beamformer weight vector:

$$\lambda_{\max} \mathbf{A} \mathbf{w} = \mathbf{B} \mathbf{w}. \quad (13)$$

Note that this fully includes mutual coupling effects, including the distortion of individual patterns.

In this equation, both \mathbf{A} and \mathbf{B} are frequency-dependent (via the EEPs) and additionally, \mathbf{B} is the scan angle-dependent. For both of these, accurately computed (or measured) EEPs over the frequency band of interest are required.

The green curve in Fig. 13 shows the station beam produced using the MAXDIR beamformer weights as in Eq. (13). The green curve fully recovers the residual squint in the beam position of the phase equalization technique and the MAXDIR beamforming also provides considerably more peak directivity (around 5 dB, a factor of around 3.1 in linear scale).

Although we have focused on directivity in this section, for a receive-only array, the SNR gain, also known as array gain, is the key parameter. The conditions under which array gain and directivity are identical are outlined in Sec. 6.1.1 of Ref. 11; in short, this neglects all noise sources other than external isotropic brightness temperature.

This section has demonstrated an approach using MAXDIR beamforming which can improve the performance of the AAVS2 (and by implication, SKA-Low). The effect on directivity is most significant at 50 MHz, the bottom end of its frequency coverage. It has been shown that this beamforming approach can correct both the pointing error and loss of directivity. However, this comes with some computational cost. It is also clear from the results presented that the phenomena of beam squint and loss of directivity are only a significant problem at the lowest operating frequency of AAVS2 (viz. 50 MHz), and then only when scanned to the 45-deg limit in the E plane. By 70 MHz, both issues are far less prominent, and above 100 MHz, the effects are hardly noticeable. Thus when operating in the frequency range critical to epoch of reionization (EoR) science, the simple geometric phasing strategy should work acceptably. This is not however the case for cosmic dawn science, which is conducted at frequencies below the EoR. As such, the current approach based on geometric phasing should be adequate for at least the initial release of the proposed AA0.5 array for EoR work. (The AA0.5 array is planned to comprise six full preproduction SKA-Low stations, to permit further testing, in particular of interstation correlation.)

7 Station Sensitivity

From an EM point of view, one of the most important requirements for SKA-Low is the antenna sensitivity. The sensitivity thresholds indicated in the requirement 2135 are given at zenith direction, while requirement 2622 (present in the previous release of the SKA requirements but now replaced with the average—see Sec. 9.1) indicated that the sensitivity shall not degrade by more than 30% at local elevation angle of 60 deg and not by more than 50% at local elevation angle of 45 deg compared to the peak sensitivity at zenith.

The sensitivity is computed following the prescription given in Ref. 41, which are briefly summarized hereafter. The sensitivity as a function of the spherical coordinates (θ, ϕ) is given by

$$\text{sensitivity}(\theta, \phi) = \eta_{\text{dig}} \frac{A_{\text{eff}}(\theta, \phi)}{T_{\text{sys}}}, \quad (14)$$

where the effective area $A_{\text{eff}}(\theta, \phi)$ is proportional to the station directivity multiplied by the radiation efficiency (η_L). In this contribution, the effective area has been evaluated both for the

isolated case (which provides a simplified value but with high-frequency resolution) and then computed for the full station in a few frequency points in order to provide accurate results accounting for the mutual coupling. The denominator of Eq. (14) represents the system noise temperature (T_{sys}) which is the sum of three contributions as follows.

The first contribution is from the antenna temperature, which is the spatial integral of the sky brightness distribution multiplied for the station pattern. Since the sky noise temperature is given⁴¹ as averaged in the whole sky, the antenna temperature coincides with the brightness temperature. The second contribution is from the physical temperature of the antenna multiplied by $(1 - \eta_L)$; and the final contribution is from the receiver noise temperature, which is the input noise temperature of the LNA (in the SKALA4.1 antenna ~ 35 K between 50 and 350 MHz), plus the noise contribution of the receiving chain after the LNA (assumed equal to 12,000 K) divided by the LNA transducer gain computed with the amplifier connected to the real antenna impedance (see Fig. 3 of Ref. 3).

Finally, the sensitivity also takes into account the efficiency of the signal processing system (η_{dig}) assumed equal to 98%.

The station sensitivity is calculated for each observation point. In Fig. 14, the sensitivity is expressed against frequency as maximum value (occurring at zenith direction) and minimum value (occurring around 45 deg zenith angle in the E plane). The same plot also shows the average of the sensitivity across the FoV. The latter shows that the distribution of the sensitivity over the FoV is closer to the maximum values rather than to the minimum ones.

The two plots of Fig. 14 are computed using one single polarization (a) or averaging the two polarizations for each direction (b). This averaging, made in order to take into account the behavior in both polarizations, has no effect in the maximum of the sensitivity, while it raises the minimum values because it mitigates the low sensitivity of the E plane by the corresponding value of the H plane for the other polarization.

The blue envelope and blue curve indicate the sensitivity computed from the isolated pattern, while the dots provide the sensitivity computed by using EEPs for the frequencies listed in Table 1. Overall, the agreement between the two sensitivity approaches is good, which means that the mutual coupling does not particularly impact on the sensitivity. On the other hand, especially for the minimum values, the rigorous approach below 100 MHz provides quite different values with respect to the isolated case, which could be attributed to the strong mutual coupling. The fast ripple in the maximum of the sensitivity for the isolated approach is due to the measurement errors in the noise temperature of the LNA.

Finally, Fig. 14 includes also the SKA requirement levels given at zenith and 45 deg off zenith. It is possible to appreciate that while the computed maximum level is always larger than

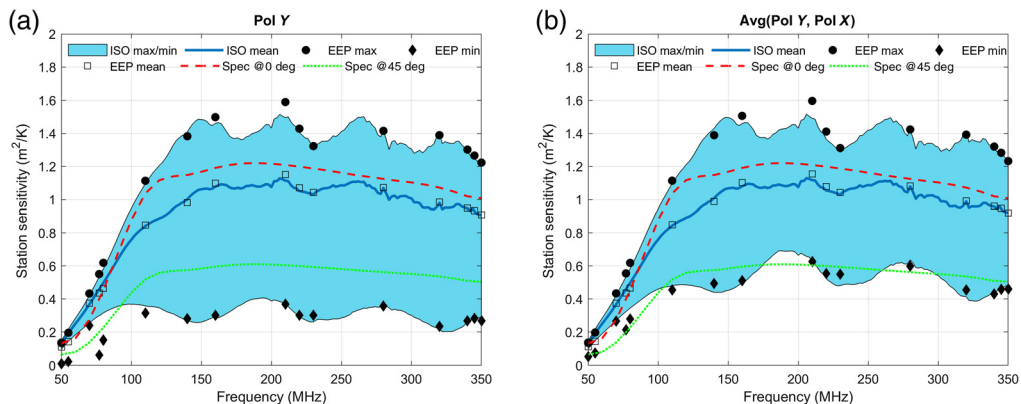


Fig. 14 Minimum/maximum sensitivity versus frequency for the station beams computed using the AF approach (blue envelope) and using the EEP formulation (diamonds and circles, respectively) for every pointing up to 45 deg zenith angle. The averages of the sensitivities throughout the FoV are also shown (continuous blue line for the AF and rectangles for the EEP). (a) Only one polarization has been considered and (b) the two polarizations have been averaged along each direction. The plots also include the SKA sensitivity requirements at zenith (red dashed curve) and at 45 deg from zenith (green curve).

the threshold, at 45 deg the estimated numerical performance shows a limited sensitivity with respect to the scientific requirements (basically due to the E plane response of the SKALA4.1 antenna). However, by averaging the two polarizations, the computed sensitivity for 45 deg off zenith angle oscillates around the threshold [see Fig. 14(b)]. Note that this approach is based on a narrow field of view approximation; recent work on off-zenith sensitivity quantifies the error made by averaging polarizations at about 15% maximum at 45 deg for a single pair of dipoles, which feature a large FoV.⁴² Work is in progress on extending this to arrays.

8 Intrinsic Cross-Polarization Ratio

Carozzi and Woan⁴³ provided a comprehensive motivation for and discussion of intrinsic cross-polarization ratio (IXR) in their original paper. The key concepts will be summarized briefly here. IXR is defined as

$$\text{IXR} = \left(\frac{\kappa(\mathbf{J}) + 1}{\kappa(\mathbf{J}) - 1} \right)^2. \quad (15)$$

Here \mathbf{J} is the Jones matrix, which gives the measured Jones vector at the polarimeter output \mathbf{f} , in terms of the true Jones at the polarimeter input \mathbf{e} , according to

$$\mathbf{f}(\omega, \vec{s}) = \mathbf{J}(\omega, \vec{s})\mathbf{e}(\omega, \vec{s}), \quad (16)$$

where ω is the angular frequency, and \vec{s} is the direction of incidence ($-\vec{r}$ in the spherical coordinate system). $\kappa(\mathbf{J})$ is the condition number of the Jones matrix. Bold symbols here represent a vector quantity in the linear algebra sense.

Both the true and measured Jones vectors are defined with respect to appropriate coordinate systems. These need not be the same, and in the following, the Jones matrix that will be assembled from numerical simulation has the form

$$\mathbf{J}(\omega, \vec{s}) = \begin{pmatrix} E_{\theta Y} & E_{\phi Y} \\ E_{\theta X} & E_{\phi X} \end{pmatrix}. \quad (17)$$

Here X and Y are the polarimeter channels, as before, and $E_{\theta Y}$, $E_{\phi Y}$ etc. are the usual field components in the spherical coordinate system. These fields can be most easily obtained from a transmission analysis (i.e., the array is driven at its ports). There are multiplicative constants in the channels that cancel and are hence omitted here.⁴⁴ A detailed discussion of obtaining antenna reception properties from radiated fields may be found in Sec. 5.1.2 of Ref. 11.

For the AAVS2 array, the IXR has been computed by phase steering the beam in every direction (the cone 45 deg from zenith for SKA-Low) and for each pointing the IXR at the nominal maximum direction has been extracted. Finally, the smallest IXR value in the whole angular section has been found. This can be a relatively computationally demanding process; for angular resolution of the order of a degree, this takes several hours on a typical personal computer, per frequency point. Faster methods could be sought, but this analysis needs only be undertaken once so speed is not essential. Results are presented in Table 2. The Galileo and FEKO IXR results are not identical, as can be expected from the results presented in Sec. 5. This is due both to minor differences in the models used (discussed in Sec. 3) and different angular resolutions. All the computed minimum IXR values tabulated occur at $\theta = 45$ deg, the maximum specified scan angle for SKA-Low. It is worth noting that IXR generally degrades very rapidly for larger scan angles.

Figure 15 shows the IXR computed by steering the array beam in every single direction and extracting the IXR at that specific angle. The IXR are plotted as UV maps for four different frequencies: 50, 70, 160, and 350 MHz. Overall, at 160 and 350 MHz, the two maps are quite similar and the IXR values at the edge of the FoV (corresponding to the magenta circle) are above 10 dB. At lower frequencies, IXR behaves very differently with excellent performance at 70 MHz (more than 20 dB) and very low values (down to <5 dB) at 50 MHz.

Table 2 Minimum IXR for the AAVS2 as computed by Galileo and FEKO.

Frequency (MHz)	Galileo (dB)	FEKO (dB)
50	2.6	3.0
55	4.9	5.2
80	9.5	10.4
140	11.7	13.0
160	12.2	12.6
230	11.4	11.6
350	12.7	13.4

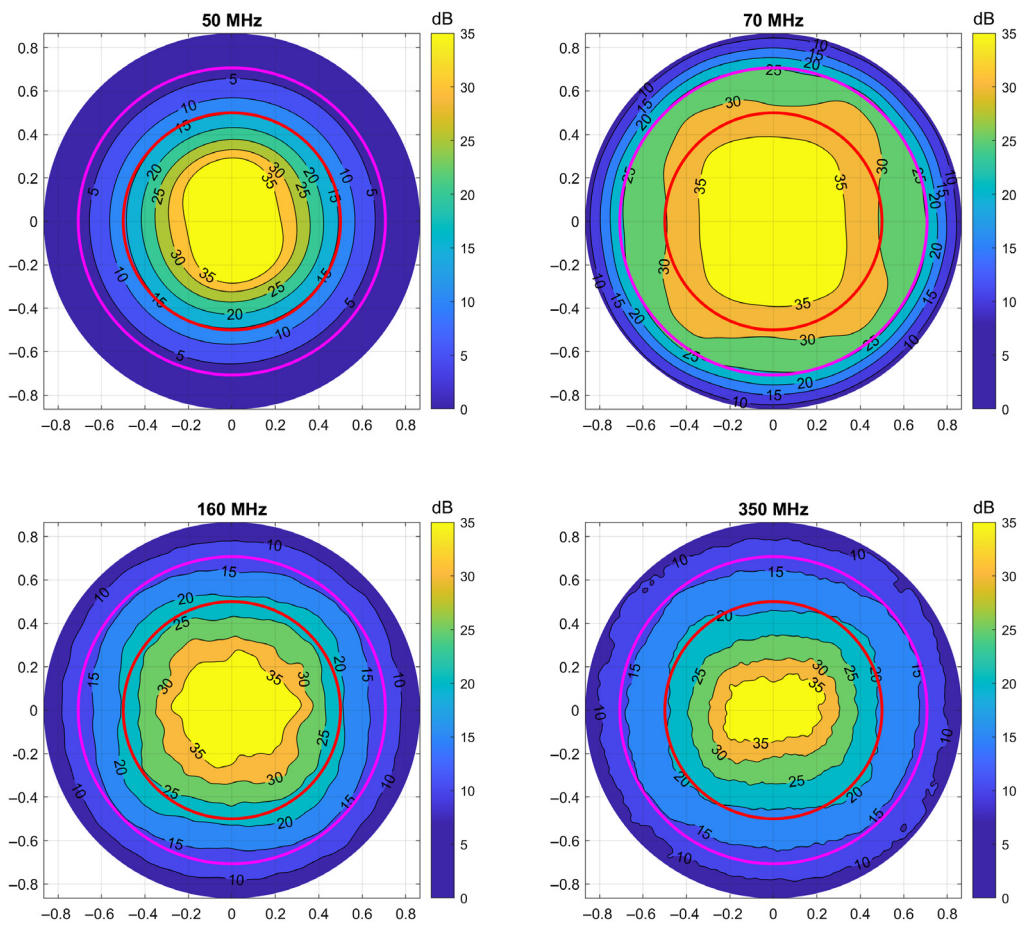


Fig. 15 UV maps of the IXR performance for four different frequencies computed for AAVS2 using the EEPs. The UV maps are computed up to 60 deg off zenith angle, while the red and magenta circles indicate the zenith angle of 30 deg and 45 deg, respectively. The maps have been compressed to 35 dB maximum to highlight low IXR values.

9 Lessons Learned and the Impact on the SKA-Low

The challenge facing by the SKA-Low telescope designers, i.e., observing the sky as never been done before, is reflected in the extremely demanding requirements.⁴⁵ Many of these are complex to verify. In such an environment, the knowledge of the instrument and its calibratability play a fundamental role, in which prototyping activities, and in particular station prototypes, are essential.

The competing requirements of both high and uniform sensitivity across a 7:1 bandwidth, and on stability of spectral response across the same band, have driven up the electromagnetic complexity of the individual antennas. This has been identified as one of the main risks. This is especially so since the antennas are arranged in a tightly packed configuration, leading to mutual coupling effects that complicate the antenna complex gains and therefore the overall station beamforming. It was therefore required to measure and assess cross-talk against the requirements and, at the same time, to perform a requirements review and a reassessment of compliance supported by station-level tests.⁴⁶

9.1 Sensitivity Requirements

Sensitivity requirements for the SKA-Low telescope have been directly derived from the science requirements.⁴⁷

Initially, feasibility and compliance against such requirements were mostly based on ideal formulations and simulations, including a rough estimation of the transition frequency from dense to sparse regime, the use of different formulations for the two different regimes, and the use of the gain of an isolated antenna multiplied by the total number of the antennas of the array. The electromagnetic simulation work carried out as part of AAVS2 has permitted a far better understanding of the station's behavior and has consequently increased the accuracy of sensitivity calculations.⁴⁸

The sensitivity requirements themselves, while maintaining the required minimum values, have been better specified and worded as a consequence of this work. For example, there is now an explicit mention of taking the average in polarization (previously missing) to take into account differences in values among the two polarizations.⁴⁵

The realistic behavior of the antenna and the station has also been, in part, taken into account by not specifying the requirement only in two off-zenith directions (30 deg and 45 deg from zenith), but rather constraining the average sensitivity within the overall FoV,⁴⁵ in order to address anomalous behavior in certain scanning directions.

The work on the AAVS2 has represented a fundamental step in improving the awareness in terms of compliance statements and verification, as described in Sec. 7 and Ref. 20. Further work to guarantee and better address the required spectral smoothness is in progress.

9.2 Polarization Requirements

The polarization requirements for the SKA-Low are expressed in terms of polarization dynamic range and cross-polarization purity. In particular, with reference to the latter, the IXR, outlined earlier in this paper, has been chosen as figure of merit.⁴³

The original polarization requirement was expressed in terms of 15 dB of minimum IXR over the whole observing band within the HPBW and up to observing angles of 45 deg off-zenith. Although the 15-dB threshold could have been achieved over much of the frequency range and FoV, it became clear that, due to projection effects (i.e., loss of orthogonality between pairs of dipoles at large incident angles) and in conjunction with the directivity required by the antenna itself, this requirement was overly stringent and unattainable at low frequencies and at the edge of the FoV.

The simulation work undertaken on AAVS2 has shown a strong effect of mutual coupling at frequencies below 100 MHz at the edge of the FoV where noncompliance with the original requirement is most prominent (Sec. 8).

This AAVS2 simulation work has also exposed the need to review the algorithm used to calculate the IXR and to link such algorithm to the IXR requirement itself to uniquely assess compliance; IXR is a relatively new metric, hence the need to be prescriptive in this regard. The actual algorithm now used in evaluating IXR for AAVS2 scans a station beam across the sky and, for each pointing, determines the minimum IXR within the HPBW of the station beam.

The necessity of moving toward a more feasible requirement in order to best reflect the SKA-Low science objectives and SKA-Low antenna physics has been recognized in the past years as simulation work has progressed. The work undertaken has resulted in a more attainable requirement of 11 dB instead of 15 dB across the whole band.

Moreover the need to take into account the realistic behavior of the full station is now reflected into the most recent revision of requirements, by explicitly mentioning, together with the minimum value of 11 dB, that this value refers to the actual station beam, where mutual coupling effects are included.

The proposed approach to polarization (Jones) correction for the SKA-Low system assumes the use of simulation and calculation to develop Jones-matrix correction terms for each signal chain based on its EEP, in order to correct the polarization seen at that element and reduce the error in X , Y to the nominal IXR behavior. This model can be validated to some level with direct measurement (i.e., drone flights) for a representative case. The model will be assumed to represent the behavior rather than relying on active correction. Although the Jones-matrix predicted values can be indeed readily extracted from EM simulations, the measurement and analysis techniques to verify the accuracy of corrections using these parameters are in an embryonic state and a practical plan for measuring and validating polarization (Jones) corrections requires further development.

Further simulation work will include: a deeper analysis of SKALA4.1 antenna tolerances and misalignment and their effect on the IXR of the antennas; further consideration of the demonstration and verification of polarimetric corrections at the antenna level—which is a particularly difficult problem; and further improvement in terms of the polarization requirements and their verification (e.g., specifying the IXR calculation method to be used for the values provided).

9.3 Stability and Reproducibility of an SKA-Low Station

Currently used calibration methods usually assume that the directional response of the receiving antenna elements is identical. This approach ignores the mutual coupling effects between the receiving elements in an irregular configuration, such as the one in the SKA-Low, and leads to systematic errors in the calibration results, where the magnitude of these errors increases with increasing EEP variations. Therefore, one of the main objectives of the AAVS2 effort has been to derive and validate EEPs, which can be used in calibration calculations. At the same time, research is ongoing to incorporate the EEPs into station calibration algorithms and to develop efficient and accurate simplified representations of the patterns.^{49,50}

The overall stability and reproducibility of SKA-Low station beam behavior is difficult to validate by actual measurements. A realistic simulation of station behavior, based on physical models of station components, that can be validated by measurements, would therefore be a valuable tool for assessing expected station beam behavior in practical conditions. Important work is ongoing at system level on this regard.⁵¹ In particular, simulations of the EEPs, together with the results of the analysis of AAVS2 components in the receiver chain (including for example a temperature model of the receiving chain of AAVS2) have been already used as part of the input data to a system model simulating the response of a single station. This model, based on a realistic behavior of station components, supports on-going work to better understand and assess the calibratability of SKA-Low, generating functions to calculate full-polarization station beams and intrastation visibilities. These can either include the gain distortions or emulate a perfectly calibrated system.

Next steps of this system level analysis will include the use of realistic antenna responses based on EM-simulations validated by drone measurements on the AAVS2 prototype system. This will permit the analysis to either include data for individual EEPs for each antenna or to use the average EEP provided by the EM-simulations.

All this work will lead eventually to possible further improvement on stability and beam accuracy requirements and their verification as well as the overall calibration strategy. Ultimately, these system-level simulations, fed by AAVS2 simulation work and measurements, will contribute in building the confidence that SKA1-Low can satisfy its science requirements.

10 Conclusions

Work on the AAVS2 SKA-Low prototype has spanned a wide variety of activities, from theoretical studies to the issues of deployment on remote sites. This paper has focussed on computational electromagnetic simulation of the prototype station. Using accelerated MoM solvers

(specifically the MLFMM), we have been able to develop rigorous full-wave electromagnetic models of this complex system for two different EM solvers. We have cross-verified the results, and shown that apart from one or two problematic frequencies, we obtain excellent agreement between these independently generated CAD models; generating models independently is an important part of verification, as otherwise the same error can occur in both models. The core data output is a set of EEPs, and we have discussed how the station beam can be synthesized from this. Both traditional array-factor-based methods, as well as a technique from beamforming theory, have been demonstrated. From the station beam, cross-polarization has been investigated via the IXR metric. Another core output is the array scattering parameter matrix, and results for this have also been shown.

This paper has concluded with a discussion of the impact of the CEM modeling activities on the SKA-Low project.

11 Appendix A. Embedded Element Patterns and Terminating Impedances

Some care is needed when using EEPs for an array such as AAVS2, both due to the different conventions in the literature for choosing terminating impedances on all the nonfed antennas, and also due to considerations for receive antennas, where reciprocity must be carefully applied in the context of receiver with active elements (typically LNAs). In this section, some of the subtleties related to EEPs are briefly reviewed.

The original definition of EEPs (then called active element patterns³⁷) assumed matched loads terminating all the nonfed antennas. In this case, the appropriate sum for the radiated field is in terms of feed voltages and matched load terminated EEPs:

$$\vec{E}(\vec{r}) = \sum_{n=1}^N v_n \vec{E}_n^{Z_g}(\vec{r}) e^{jk(\xi_n - \alpha_n)}, \quad (18)$$

where the EEP now explicitly displays the Z_g notation of Refs. 11 and 52. It is assumed that all the loads are the same Z_g . More recently, open-circuit (OC) referenced EEPs have been introduced.^{11,53} For this convention, the radiated field is given in terms of port currents and OC terminated embedded elements:

$$\vec{E}(\vec{r}) = \sum_{n=1}^N i_n \vec{E}_n^{\text{oc}}(\vec{r}) e^{jk(\xi_n - \alpha_n)}. \quad (19)$$

The feed voltages and port currents are related by

$$\mathbf{i}_A = (\mathbf{Z}_g + \mathbf{Z}_A)^{-1} \mathbf{v}_g, \quad (20)$$

where \mathbf{i}_A is the vector of port currents, \mathbf{Z}_A is the array mutual impedance matrix, \mathbf{Z}_g is the source impedance matrix (usually diagonal), and \mathbf{v}_g is the vector of Thévenin equivalent feed voltages, following the notation of Chapter 4 of Ref. 11. Formulas have been derived using Eq. (20) to transform between OC, short-circuit, and matched-load terminations and are available in the literature.⁵²

On reception, the EEPs themselves are reciprocal. However, for an active array, one needs to exercise caution with reciprocity, as elements of the receiver chain (in particular the LNA) are nonreciprocal. It may be shown that the receiving network and the array mutual impedance matrix (which on receive is the transpose of that on transmit⁵²) loads the array elements, and the port voltages (which are what traverse the receiver chain to the beamformer) are proportional to the matched EEPs.⁵² As such, the voltage at the output of the array beamformer is proportional to the weighted sum of the matched-load EEPs (as plotted in this paper). This is a subtle point not immediately obvious for receive-only systems.

Note that it is also assumed in Eq. (18) that for each antenna, the phase term related to the antenna position is not included in \vec{E}_n . Some of the literature includes this phase term within the

EEP, but usage is not always consistent. For large arrays such as the AAVS2, keeping the phase term separate can be advantageous in terms of storage. In essence, in this approach, the complex field response of each antenna is combined with the geometrical delays imposed by the AF. In one of the original references on EEPs (called active elements at the time),³⁷ the term “phase-adjusted” was used for this approach.

For the MAXDIR beamformer, there is another subtlety which should be noted for the receive case. The EEPs in Eqs. (8)–(13) are EEPs referenced to OC terminations, and the weights which emerge from the eigenvalue solver are also OC referenced. The EEPs and weights can both be transformed to matched terminations. Transformations using the array mutual impedance matrix are available to transform either the matched-load EEPs to OC EEPs [Ref. 52, Eq. (4)], or similarly for the weight vector [Ref. 11, Sec. 5.1.4]. When either the OC weights and OC EEPs, or the matched weights and matched EEPs, are multiplied to form the beam as in Eq. (8), these transforms have terms that cancel (within a constant). Hence, the beam can be formed from either product.

Another point worth mentioning is the role of r (distance from the origin) in the computation of the EEPs. If the appropriate constants are retained [Ref. 11, Chapter 4], the EEPs give the electric field directly at distance r from the origin. However, many formulations instead compute fields at a nominal distance—for instance FEKO and Galileo suppress the e^{-jkr}/r term when computing fields. Although the absolute field values of the EEPs are not essential, the relative field values are, and the same nominal distance (and source voltage) must be used in computing each EEP. For this reason, we retain \vec{r} in Eq. (6). The plots in this paper show directivity of the EEPs and station beams; this has been obtained from the computed fields using the basic definition of directivity,³⁸ where the actual value of r cancels; numerical integration of the computed fields has been used to evaluate the total radiated power.¹¹

Finally, note that an EEP is a field-related quantity, with both amplitude and phase. This is especially convenient for interferometry, as these are the “voltage beams” in radio astronomy terminology. It will be appreciated that storing the 512 EEPs (256 per polarization) for AAVS2 over a large number of frequency points requires a very significant amount of storage. The use of compressed storage for low-frequency radio astronomy arrays was addressed in the context of a LOFAR low-band station,⁵⁴ and more recently this has been considered in the context of SKA prototype stations.⁵⁰

Acknowledgments

AAVS2 is hosted by the MWA under an agreement via the MWA External Instruments Policy. This scientific work makes use of the Murchison Radio-astronomy Observatory, operated by CSIRO. We would like to acknowledge the Wajarri Yamatji people as the traditional owners of the observatory site.

References

1. P. Benthem et al., “The aperture array verification system 1: system overview and early commissioning results,” *Astron. Astrophys.* **655**, A5 (2021).
2. A. van Es et al., “A prototype model for evaluating SKA-Low station calibration,” *Proc. SPIE* **11445**, 1144589 (2020).
3. P. Bolli et al., “Test-driven design of an active dual-polarized log-periodic antenna for the Square Kilometre Array,” *IEEE Open J. Antennas Propag.* **1**, 253–263 (2020).
4. Altair Engineering Inc., “Altair Feko v.2021,” www.altair.com/feko (2022).
5. Ingegneria Dei Sistemi S.p.A., “Galileo suite,” <https://www.idscorporation.com/pf/galileo-suite/> (2022).
6. D. B. Davidson et al., “Electromagnetic modelling of the SKA-LOW AAVS1.5 prototype,” in *Int. Conf. Electromagn. Adv. Appl. (ICEAA)*, pp. 1032–1037 (2019).
7. D. Davidson et al., “Electromagnetic modelling of the SKA-LOW AAVS2 prototype,” in *XXXIII Gen. Assembly and Sci. Symp. (GASS) of the Int. Union of Radio Sci. (URSI)* (2020).

8. F. Paonessa et al., “First results on the validation of the SKA-Low prototypes using an airborne test source,” in *XXXIII Gen. Assembly and Sci. Symp. (GASS) of the Int. Union of Radio Sci. (URSI)* (2020).
9. F. Paonessa et al., “SKA-Low prototypes deployed in Australia: synoptic of the UAV-based experimental results,” *Radio Sci. Lett.* **2**, 1–5 (2020).
10. T. Bird, *Mutual Coupling Between Antennas*, Wiley, New York (2021).
11. K. F. Warnick et al., *Phased Arrays for Radio Astronomy, Remote Sensing, and Satellite Communications*, Cambridge University Press, Cambridge (2018).
12. M. P. van Haarlem et al., “LOFAR: The LOW-Frequency ARray,” *Astron. Astrophys.* **556**, A2 (2013).
13. S. W. Ellingson et al., “The long wavelength array,” *Proc. IEEE* **97**(8), 1421–1430 (2009).
14. S. J. Tingay et al., “The Murchison widefield array: the Square Kilometre Array precursor at low radio frequencies,” *Publ. Astron. Soc. Aust.* **30**, e007 (2013).
15. D. Isbell, “Log periodic dipole arrays,” *IRE Trans. Antennas Propag.* **8**(3), 260–267 (1960).
16. E. de Lera Acedo et al., “SKALA, a log-periodic array antenna for the SKA-Low instrument: design, simulations, tests and system considerations,” *Exp. Astron.* **39**, 567–594 (2015).
17. E. de Lera Acedo et al., “Evolution of SKALA (SKALA-2), the log-periodic array antenna for the SKA-Low instrument,” in *Int. Conf. Electromagn. Adv. Appl. (ICEAA)*, pp. 839–843 (2015).
18. E. de Lera Acedo, H. Pienaar, and N. Fagnoni, “Antenna design for the SKA1-Low and HERA super radio telescopes,” in *Int. Conf. Electromagn. Adv. Appl. (ICEAA)*, pp. 636–639 (2018).
19. Sirio Antenne, “Company website,” <https://www.sirioantenne.it/en/> (2022).
20. G. Macario et al., “Characterization of the SKA-Low prototype station Aperture Array Verification System 2,” *J. Astron. Telesc. Instrum. Syst.* **8**(1), 011014 (2022).
21. M. Sokolowski et al., “Preliminary sensitivity verification of the SKA-Low AAVS2 prototype,” in *15th Eur. Conf. Antennas Propag. (EuCAP)*, pp. 1–5 (2021).
22. M. Sokolowski et al., “A southern-hemisphere all-sky radio transient monitor for SKA-Low prototype stations,” *Publ. Astron. Soc. Aust.* **38**, e023 (2021).
23. D. B. Davidson, *Computational Electromagnetics for RF and Microwave Engineering*, 2nd ed., Cambridge University Press, Cambridge (2011).
24. S. Rao, D. Wilton, and A. Glisson, “Electromagnetic scattering by surfaces of arbitrary shape,” *IEEE Trans. Antennas Propag.* **30**, 409–418 (1982).
25. R. Coifman, V. Rokhlin, and S. Wandzura, “The fast multipole method for the wave equation: a pedestrian prescription,” *IEEE Antennas Propag. Mag.* **35**(3), 7–12 (1993).
26. V. V. S. Prakash and R. Mittra, “Characteristic basis function method: a new technique for efficient solution of method of moments matrix equations,” *Microwave Opt. Technol. Lett.* **36**(2), 95–100 (2003).
27. L. Matekovits, V. A. Laza, and G. Vecchi, “Analysis of large complex structures with the synthetic-functions approach,” *IEEE Trans. Antennas Propag.* **55**(9), 2509–2521 (2007).
28. R. Maaskant, R. Mittra, and A. Tjihuis, “Fast analysis of large antenna arrays using the characteristic basis function method and the adaptive cross approximation algorithm,” *IEEE Trans. Antennas Propag.* **56**(11), 3440–3451 (2008).
29. H. Bui-Van et al., “Fast and accurate simulation technique for large irregular arrays,” *IEEE Trans. Antennas Propag.* **66**, 1805–1817 (2018).
30. D. J. Ludick et al., “Efficient analysis of large aperiodic antenna arrays using the domain Green’s function method,” *IEEE Trans. Antennas Propag.* **62**, 1579–1588 (2014).
31. M. Chose and M. M. Botha, “Improvements to the domain Green’s function method for antenna array analysis,” in *Int. Conf. Electromagn. Adv. Appl. (ICEAA)*, pp. 0392–0395 (2019).
32. R. Steiner et al., “Optimizing processing time of radio-astronomy antenna simulations using FEKO,” *Appl. Comput. Electromagn. Soc. J.* **35**, 1153–1160 (2020).
33. P. Bolli et al., “Preliminary analysis of the effects of the ground plane on the element patterns of SKA1-Low,” in *14th Eur. Conf. Antennas and Propag. (EuCAP)*, pp. 1–4 (2020).
34. J. Cavillot et al., “Fast simulation technique for antenna installed on a finite ground plane,” in *Int. Conf. Electromagn. Adv. Appl. (ICEAA)*, pp. 0742–0745 (2019).

35. P. Bolli et al., “Optimization of random array layout to improve spectral smoothness,” SPIE JATIS, Submitted for the SKA Observatory Special Section (2022).
36. D. B. Davidson and D. X. Ung, “Spectral smoothness of embedded element patterns in the SKA-LOW prototype station AAVS2: preliminary results,” in *IEEE Int. Symp. Antennas Propag.*, pp. 1–2 (2021).
37. D. F. Kelley and W. L. Stutzman, “Array antenna pattern modeling methods that include mutual coupling effects,” *IEEE Trans. Antennas and Propag.* **41**, 1625–1632 (1993).
38. W. L. Stutzman and G. A. Thiele, *Antenna Theory and Design*, 2nd ed., John Wiley and Sons, New York (1998).
39. P. Bolli et al., “SKA1-Low: impact of antenna response and mutual coupling on the off-zenith array pointing,” in *15th Eur. Conf. Antennas and Propag. (EuCAP)*, pp. 1–4 (2021).
40. S. J. Wijnholds et al., “Calibration challenges for future radio telescopes,” *IEEE Signal Process. Mag.* **27**(1), 30–42 (2010).
41. M.G. Labate et al., “SKA1-Low antenna statement of work,” Tech. Rep. SKA-TEL-SKO-0001651, SKAO (2017).
42. A. T. Sutinjo et al., “Sensitivity of a low-frequency polarimetric radio interferometer,” *Astron. Astrophys.* **646**, A143 (2021).
43. T. D. Carozzi and G. Woan, “A fundamental figure of merit for radio polarimeters,” *IEEE Trans. Antennas Propag.* **59**, 2058–2065 (2011).
44. B. Fiorelli and E. De Lera Acedo, “On the simulation and validation of the intrinsic cross-polarization ratio for antenna arrays devoted to low frequency radio astronomy,” in *8th Eur. Conf. Antennas and Propag. (EuCAP 2014)*, pp. 2361–2364 (2014).
45. M. Caiazzo et al., “SKA phase 1 system requirements specification (SRS),” Tech. Rep. SKA-TEL-SKO-0000008, SKAO (2017).
46. M. Waterson et al., “Report on the station calibration task,” Tech. Rep. SKA-TEL-SKO-0001088, SKAO (2019).
47. R. Braun et al., “SKA1 level 0 science requirements,” Tech. Rep. SKA-TEL-SKO-0000007, SKAO (2015).
48. M. Sokolowski et al., “What is the SKA-Low sensitivity for your favourite radio source?” PASA, Submitted (2021).
49. S. J. Wijnholds et al., “Using embedded element patterns to improve aperture array calibration,” in *Int. Conf. Electromagn. Adv. Appl. (ICEAA)*, pp. 0437–0442 (2019).
50. J. L. Jones and R. B. Wayth, “Accuracy versus complexity: calibrating radio interferometer arrays with non-homogeneous element patterns,” *Mon. Not. R. Astron. Soc.* **505**, 1485–1494 (2021).
51. S. J. Wijnholds, “Embedded element patterns in hierarchical calibration of large distributed arrays,” in *XXXIIIrd Gen. Assembly and Sci. Symp. Int. Union of Radio Sci.*, pp. 1–4 (2020).
52. K. F. Warnick, D. B. Davidson, and D. Buck, “Embedded element pattern loading condition transformations for phased array modeling,” *IEEE Trans. Antennas Propag.* **69**(3), 1769–1774 (2021).
53. D. A. Roshi, W. Shillue, and J. R. Fisher, “Model for a noise-matched phased array feed,” *IEEE Trans. Antennas Propag.* **67**(5), 3011–3021 (2019).
54. A. Young et al., “Efficient correction for both direction-dependent and baseline-dependent effects in interferometric imaging: an a-stacking framework,” *Astron. Astrophys.* **577**, A56 (2015).

Pietro Bolli received his Laurea degree in electronic engineering and his PhD in computer science and telecommunications engineering from the University of Florence, Florence, Italy, in 1999 and 2003, respectively. In 2002, he started his professional career as a microwave engineer at the Italian National Institute for Astrophysics (INAF) conducting research in the field of technology applied to radio astronomy. He is currently senior technologist at the INAF Arcetri Astrophysical Observatory. He is a co-author of about 140 scientific publications, which have appeared in international referred journals and conferences.

David B. Davidson received his PhD and DEng degrees from Stellenbosch University. In 2018, he joined Curtin University, Perth, Western Australia, where he is presently engineering director

of ICRAR. Prior to this, he was with Stellenbosch University, where he held an SKA-SA Research Chair. He is a fellow of the IEEE, and is a registered Chartered Engineer. He is an IEEE associate editor and presently serves on the Australia Telescope National Facility Steering Committee.

Mirko Bercigli received the Laurea degree in electronic engineering from the University of Florence in 2000. Since September 2000, he has been employed in the Computational Electromagnetic Laboratory, IDS Ingegneria dei Sistemi S.p.A., as a system analyst in the field of electromagnetism. He is currently the head of the “Computational Electro Magnetic Engineering.” He co-operates with several research centers such as the University of Florence, the Politecnico of Turin, the University of Pisa, the University of Siena, the University of l’Aquila, and the University of Rome in developing e.m. numerical methods. He also participated in several international programs supported by European Space Agency (ESA) and European Community (EC).

Paola Di Ninni received her physics degree in astrophysics and space physics from the University of Florence, Italy, in 2008, where she worked as a data analyst in the Physics of Matter from 2009 to 2013. She received her PhD in experimental physics from University of Siena, Italy, in 2017. She is currently working as a technologist in radio astronomy at the Arcetri Astrophysical Observatory of the National Institute of Astrophysics, Italy.

Maria Grazia Labate is the telescope engineer for the SKA1-LOW Telescope at the SKA Observatory. She received her BS and MS degrees in telecommunication engineering from the Mediterranea University of Reggio Calabria in 2005 and 2007, respectively, and her PhD in electronic engineering from the Second University of Naples in 2008. She is the author of more than 40 journal and conference papers and co-inventor of 3 patents. Her current role is to lead the technical activities of the SKA Low-frequency telescope. She is a member of INCOSE.

Daniel Ung received the BEng (EC) and MPhil (EC) from Curtin University, Perth, in 2015 and 2020, respectively. He was appointed as a support engineer at International Centre for Radio Astronomy since 2015. His research interest includes electromagnetic simulation and noise computation of phased arrays.

Giuseppe Virone received his degree in electronic engineering (summa cum laude) and his PhD in electronics and communication engineering from the Politecnico di Torino, Turin, Italy, in November 2001 and 2006, respectively. He is currently a senior researcher at the Istituto di Elettronica e di Ingegneria Informatica e delle Telecomunicazioni (IEIIT) of Italian National Research Council (CNR). He joined IEIIT as a research assistant in 2002. He coordinated more than 15 scientific projects funded by both the industry and other scientific research organizations and joined more than 30 research projects as a collaborator. He authored 43 journal papers, 134 conference papers, and 3 European patents. His activities concern the design, numerical analysis, and characterization of microwave and millimeter waveguide passive components for feed systems, antenna arrays, frequency selective surfaces, compensated dielectric radomes, and industrial sensing applications.